



LUNDS
UNIVERSITET

Structure and reactivity of surface oxides on Cu(100)

Author:

Benjamin Hagman

Supervisors:

Johan Gustafson

Lindsay R. Merte

Master Thesis

VT 2016

Div. of Synchrotron
Radiation Research

July 20, 2016

Contents

1	Introduction	5
2	Background	7
2.1	The Bravais & reciprocal lattices	7
2.2	Structure of Cu(100)	8
2.3	Physisorption & Chemisorption	9
2.4	Surface structure	9
2.5	Oxidization of Cu(100)	10
3	Method	16
3.1	Low-Energy Electron Diffraction	16
3.1.1	Setup	18
3.2	X-ray Photoelectron Spectroscopy	19
3.2.1	Peak shape	21
3.2.2	Experimental Setup	21
3.2.3	Data analysis	22
3.3	Auger Electron Spectroscopy	23
3.3.1	Setup	24
3.4	Scanning Tunneling Microscopy	25
3.4.1	Theory	25
3.4.2	Experimental Setup	28
3.5	STM-chamber	29
3.6	In-situ flow reactor	29
4	Experiment	31
4.1	STM, AES and LEED experiments	31
4.2	XPS experiments	32
4.3	In-situ flow reaction experiments	32
5	Results	34
5.1	Formation and partial reduction of the missing row structure	34
5.1.1	Formation of MR structure	34
5.1.2	Reduction of the MR structure	37
5.2	CO ₂ adsorption	42
5.3	Catalytic Activity	46
6	Discussion	48
7	Outlook	50

Acronym Page

RWGS	Reverse water-gas shift
ML [unit]	Monolayer (number of atoms on the surface)
MR	Missing row / missing row structure
STM	Scanning tunneling microscopy
LEED	Low-energy electron diffraction
AES	Auger electron spectroscopy
XPS	X-ray photoelectron spectroscopy
L [unit]	Langmuir (10^{-6} Torr x 1 second)
RGA	Residual gas analyzer
DS	Doniach-Sunjic

Abstract

Adsorption of oxygen onto Cu(100) leads to formation of a well-ordered surface structure known as the ‘missing row’ (MR) reconstruction. The aim of the work described in this thesis was to characterize the chemical properties of this MR structure, which serves as a well-defined analogue for oxidized copper surfaces used in catalysis for CO₂ hydrogenation. Specifically, the interaction of CO₂ with the MR structure has been studied and compared to measurements on the bare Cu(100) surface and on a partially-reduced MR surface prepared by exposure to H₂.

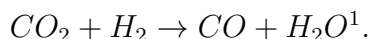
The results show that the reduction of the MR structure initially takes place at the lower terraces adjacent to step edges and at defects, producing a new phase which appears to have an amorphous structure. XPS results show a new oxygen species appearing upon reduction, which is attributed to this new structure. The XPS data further show that CO₂ sticks more strongly on the oxygen-rich surfaces than on clean Cu(100), though CO₂ adsorbs dissociatively on clean Cu(100) and the reduced MR surface, but not on the pure MR structure. Preliminary catalytic tests using an in-situ flow reactor showed conversion of CO₂ to CO above 650 °C, although the signal was weak. These results demonstrate the feasibility of further experiments using this cell for *in-situ* surface x-ray diffraction experiments to be conducted in the future.

1 Introduction

Since the industrial revolution the atmospheric concentration of carbon dioxide has increased significantly, from 280 ppm to 390 ppm (in 2010), due primarily to the combustion of fossil fuels. The concentration continues to increase rapidly [1], causing unwanted climate change as a result of the greenhouse effect.

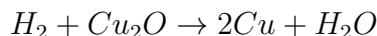
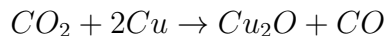
There are several possible ways to reduce the problem of increasing CO₂ in the atmosphere. One way is to use renewable energy sources, e.g. windmills and solar panels, instead of fossil fuels. Another strategy is to capture CO₂ from the atmosphere or from combustion exhaust and store it in the form of e.g. a compressed gas or a carbon containing mineral. Both these methods are being implemented to reduce atmospheric CO₂, but so far the effects remain insufficient. It has, however, been shown that CO₂ can be used to create carbon-based chemicals, like methanol. Such a recycling of CO₂ would not only help to solve the problem of climate change, by reducing the amount of CO₂ in the atmosphere, but also give new opportunities for the industry. Therefore, the recycling of CO₂ has received substantial interest in recent times [1, 2].

By hydrogenation, CO₂ can be transformed to other carbon-based chemicals. The first step in such a process frequently consists of conversion of CO₂ to CO via the reverse water-gas shift reaction (RWGS) [1, 2],



Though the gas phase reaction of CO₂ with H₂ is too slow to be useful, through introduction of a catalyst it is possible to get an activity suitable for industrial purposes [1].

Copper-based catalysts are active for both the water gas shift and reverse water gas shift reactions and are already in industrially for e.g. H₂ production [3]. However, the RWGS reaction mechanism over copper surfaces is disputed. One model is the redox mechanism which can be written as



In this process, the CO₂ first reacts with the copper, oxidizing it and then leaving as CO. Subsequently, the H₂ reduces the oxide back to metallic copper, producing water. However, other mechanisms have been proposed, such as formate (HCOO) decomposition, where CO₂ first reacts with an adsorbed hydrogen atom to form HCOO, which then decomposes to form CO [4], i.e.



The goal of this project was to achieve a better understanding of the reaction mechanisms for the RWGS reaction. To achieve this, the ‘surface science approach’ is employed,

¹Note that the chemical process can also be done in the reverse direction, i.e. carbon monoxide with water create hydrogen and carbon dioxide, which is simply referred to water-gas shift.

where a well-defined ‘model’ catalyst is used in place of the complex materials used industrially and the catalyst surfaces are characterized under well-controlled exposures to the relevant components of the reaction mixture, in this case H_2 and CO_2 in particular. Operation of the redox mechanism, for example, requires that CO_2 must be able to react with and oxidize the copper surface and H_2 must be able to reduce the surface oxides that are formed. It has been proposed that a combination of oxide sites and metallic sites is necessary, such that CO_2 adsorbs onto the oxide and H_2 onto the metal. Some previous work in this direction has already been performed:

It was shown by Yang, *et. al.* that a surface oxide on Cu(111) can be reduced by CO, forming an intermediate phase between Cu_2O and clean copper. They found that the reduction of the surface oxide can be divided into two parts: one slow reaction occurring initially and a fast reaction taking place subsequently. The slow reaction was found to consist of CO reacting with oxygen within the surface oxide. CO, however, has a low sticking probability on the well-ordered surface oxide, severely limiting the rate of the reaction. However, after some time, an oxygen deficient structure was formed and propagated on the surface. The oxygen deficient structure was found to have a higher sticking probability of CO, allowing it to react more readily with surface oxygen [5].

The goal of the present project was to study the structures of oxygen on Cu(100), as well as the intermediate phases present on the surface during the reduction process, with the aim of understanding the role of surface oxygen in the RWGS reaction. Compared to Cu(111), where several complex surface oxide phases form whose structures have still not been established definitively [6], Cu(100) is a simpler model surface, the oxygen structures forming on which (to be discussed below) have been studied in detail. The project is divided into three main parts. The first part is focused on the surface oxide its reduction by H_2 to an intermediate phase. The second part is focused on the interaction of CO_2 with the surface oxide, the intermediate reduced surface and clean Cu(100). The third task was to investigate the catalytic activity of Cu(100) using a high pressure flow reactor. This part serves as a preliminary study for future *in-situ* investigations.

2 Background

In this section, the background information from previous studies of the system of interest in this thesis will be presented. Some of the concepts that are needed for understanding the science behind this thesis will be briefly explained.

2.1 The Bravais & reciprocal lattices

In a crystal, the atoms are arranged periodically, so that its structure can be described by a Bravais lattice. The definition of the Bravais lattice is an array of points in space, arranged such that any vector

$$\mathbf{R} = m_1\mathbf{a}_1 + m_2\mathbf{a}_2 + m_3\mathbf{a}_3,$$

where m_1 , m_2 , and m_3 are integers, connects two lattice points [7, 8]. \mathbf{a}_1 , \mathbf{a}_2 and \mathbf{a}_3 are the vectors spanning the Bravais lattice. To completely describe a crystal each lattice points is associated with one or more atoms, which comprise the crystal ‘basis’. To completely describe a crystal structure only the vectors spanning the Bravais lattice (length and direction) and the basis need to be defined. For a crystalline surface, which is periodic in only two dimensions, it is only necessary to use \mathbf{a}_1 and \mathbf{a}_2 as the in-plane vectors that span the surface lattice. The combination of the atomic basis and the lattice vectors yields the crystal’s ‘unit cell’ which tiled two- or three-dimensionally produces the entire crystal. The smallest unit cell that can be chosen is called the primitive unit cell. Occasionally, non-primitive unit cells are chosen to better reflect the symmetry properties of the structure.

Another important concept, and related to the Bravais lattice, is the reciprocal lattice. The reciprocal lattice is essential for understating diffraction patterns, as will be further discussed in Section 3.1. For a 2D Bravais lattice, the reciprocal lattice is defined as all points connected by the so-called unit vectors

$$\mathbf{G} = h\mathbf{b}_1 + k\mathbf{b}_2$$

for surface lattices, with

$$\mathbf{a}_i \cdot \mathbf{b}_j = 2\pi\delta_{ij} \Leftrightarrow |\mathbf{a}_i| |\mathbf{b}_j| \cos\varphi = 2\pi\delta_{ij}, \quad (1)$$

and h , k and l being integers [7, 8]. φ is the angle between the two vectors, and δ_{ij} is the Kronecker delta function.

On the left-hand side of the equation, only one term can be zero: the cosine function. This implies that the angle between \mathbf{b}_1 and \mathbf{b}_2 has to be 90° for equation (1) to be logically correct. If the direction of every vector in \mathbf{R} is known, the directions of all the vectors in \mathbf{G} can be found by considering that the vectors with different i and j are perpendicular to each other. The length of the vectors can then be calculated by

$$|\mathbf{b}_i| = \frac{2\pi}{|\mathbf{a}_i| \cos(\varphi)}$$

The opposite case is also true: if one knows all the vectors in \mathbf{G} one can determine the real space lattice vectors.

2.2 Structure of Cu(100)

The copper crystal has a face-centered cubic (FCC) unit cell, see Figure 1(a), which has a cubic structure with atoms at the corners and the centers of the faces. Depending on how the crystal is cut different surfaces will be created. Not only will the surfaces have different symmetries but also different electronic properties and, therefore, different chemical properties [9].

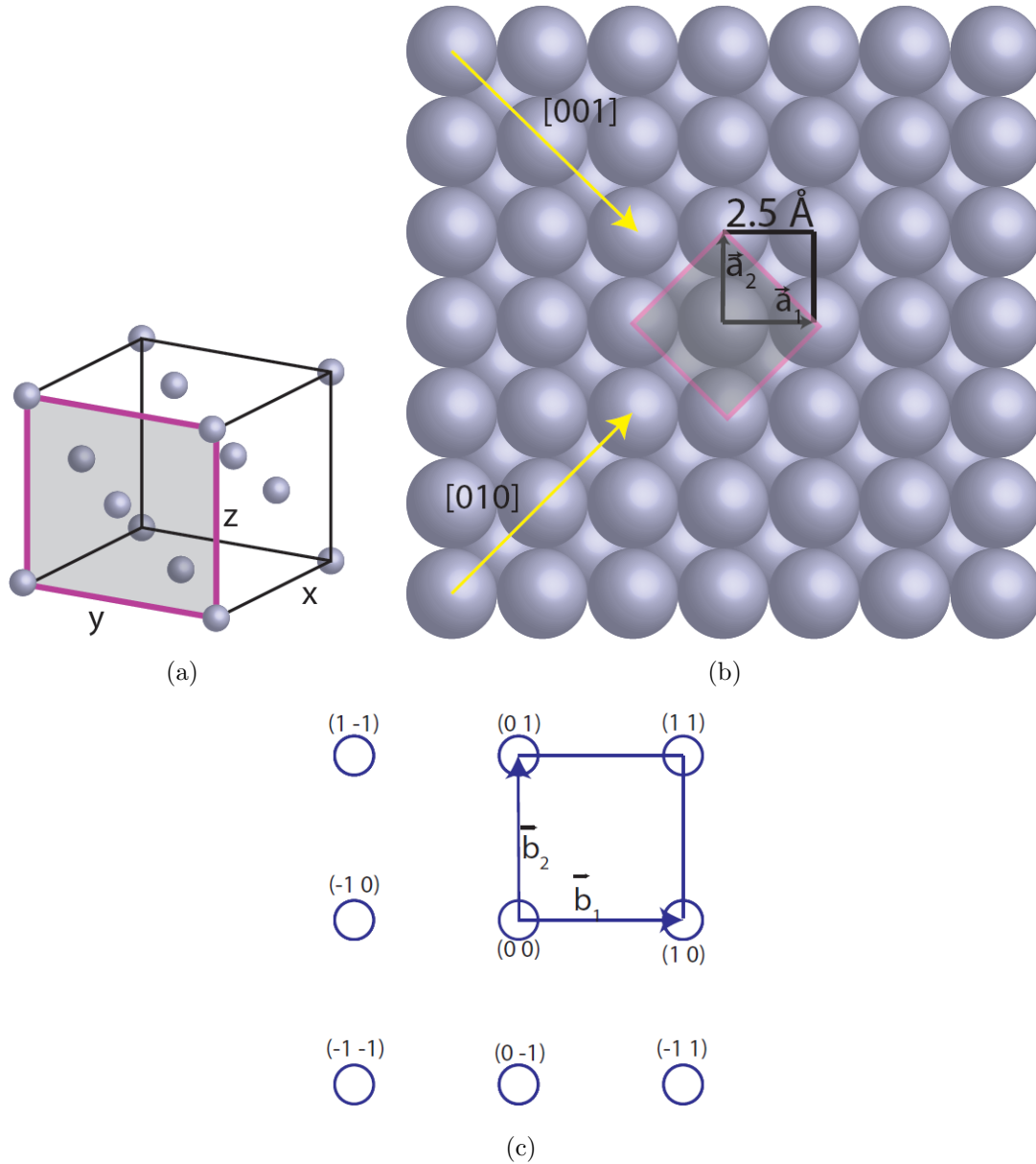


Figure 1: (a) The FCC unit cell with the (100) plane indicated. (b) The Cu(100) surface with the bulk (pink) and surface (black) unit cells and bulk lattice directions indicated. The surface unit cell is a square with an edge length of 2.5 Å. The yellow arrows indicate the [010] and [001] directions. (c) The reciprocal lattice of the Cu(100) surface. The reciprocal lattice vectors \mathbf{b}_1 and \mathbf{b}_2 is shown as blue arrows.

To describe the orientation of a surface, the Miller indices, consisting of three integers, is used to denote the plane along of which the crystal is cut. To determine the

Miller index of a plane in a cubic structure, with perpendicular Cartesian axes x , y and z , the plane's interceptions of the axes are determined. If the plane is parallel to an axis the interception is said to be at ∞ . The reciprocals of the values of the interceptions are calculated. If the plane is parallel to an axis (such that the intercept can be said to occur at ∞), the reciprocal is said to be zero. If any of the reciprocal values is a fraction, the indexes are multiplied by an integer such that all the indexes become integers [7].

As an example of Miller indices, the plane in Figure 1(a) is considered. The plane, marked as a gray cube, intercepts at $x=1$ and are parallel to both z and y . Thus, the interception is $(1\infty\infty)$. The reciprocal will then be (100) . The Cu surface cut along the (100) plane is written as $\text{Cu}(100)$.

The surface cut along the (100) plane is shown in Figure 1(b). The pink square in Figure 1(b) corresponds to the plane in 1(a). The unit cell of the $\text{Cu}(100)$ surface is best described by a square as seen in the figure. The bulk lattice constant is appr. 3.6 \AA for copper. By geometrical consideration, it can be seen that the size of the surface unit cell is then

$$|\mathbf{a}_1| = |\mathbf{a}_2| = a/\sqrt{2} \approx 2.5 \text{ \AA}$$

The reciprocal lattice of $\text{Cu}(100)$ is straightforward to determine. The vectors of the unit cell are perpendicular to each other and, therefore, the reciprocal lattice vectors will also be perpendicular to each other. The reciprocal vectors also point in the same direction as the real surface lattice vectors. The reciprocal lattice, with basis vectors, is shown in Figure 1(c).

2.3 Physisorption & Chemisorption

Adsorption of atoms and molecules onto surfaces is normally divided into two broad categories, distinguished primarily by the magnitude of the adsorption enthalpy [7]. Where the interactions are weak, with enthalpies corresponding to van der Waals forces, the process is referred to as “physisorption”. In a physisorbed state, exchange of electrons is low, and the change in enthalpy is typically in the same order as for condensation. For small molecules, desorption from the physisorbed state typically occurs well below room temperature. Where the interaction between the atoms or molecules and the surface is stronger, the adsorption is classified as “chemisorption”. The larger adsorption enthalpy is associated with the formation of ionic, covalent or metallic bonds, with consequently greater degrees of electron transfer or redistribution. Due to the difference of electron transfer between physisorption and chemisorption, it is typically possible to distinguish the physisorbed and chemisorbed states of a molecule with the use of XPS (as explained in Section 4.2).

2.4 Surface structure

In surface science, one often deals with overlayers on a crystalline substrate. It is, therefore, convenient to have a notation to describe the structure of the overlayers in a straightforward fashion. The most important descriptor of a surface structure is normally its

periodicity, and for this purpose Wood's notation is often used, which relates the unit cell of the overlayer to that of the substrate. In Wood's notation, the periodicity of a structure is given as

$$q \left(\frac{|\mathbf{a}_{o1}|}{|\mathbf{a}_{s1}|} \times \frac{|\mathbf{a}_{o2}|}{|\mathbf{a}_{s2}|} \right) R\Omega, \quad (2)$$

where q specifies if the overlayer lattice is primitive (p) or centered (c) [7], i.e. the unit cell is defined such that a Bravais lattice point is found at its center. If the surface overlayer lattice is primitive the "p" is often omitted. $\mathbf{a}_{o1,2}$ and $\mathbf{a}_{s1,2}$ are the surface lattice vectors for the overlayer and substrate respectively. $R\Omega$ specifies if the overlayer unit cell is rotated with respect to the unit cell of the substrate, however, it is often omitted from the notation if there is no rotation. It should be noted that this notation only works if both the vectors spanning the unit cell of the overlayer are rotated by the same angle with respect to the vectors of the substrate. In the general case, the overlayer periodicity can be described in terms of the transformation matrix which maps the basis vectors of the substrate lattice to those of the overlayer. All overlayers discussed in this thesis can be described by the Wood's notation and therefore the matrix notation will not be used.

As an example of Wood's notation, Figure 2(a) is considered. The Figure shows oxygen atoms adsorbed on the Cu(100) such that a square-like structure is formed, see the blue arrows in the Figure. The shortest distance between the oxygen atoms, or length of the units vectors, can be seen to be $|\mathbf{a}_{1,2}| \sqrt{2}$. By comparing the unit cell of the Cu(100) and the oxygen overlayer (see Figure 1(b) and the blue arrows in Figure 2(a)) it can be seen that the overlayer unit cell is rotated by 45° with respect to the unit cell of Cu(100). Thus, the Wood's notation becomes

$$q \left(\frac{|\mathbf{a}_{o1}|}{|\mathbf{a}_{s1}|} \times \frac{|\mathbf{a}_{o2}|}{|\mathbf{a}_{s2}|} \right) R\Omega = p \left(\frac{|\mathbf{a}_1| \sqrt{2}}{|\mathbf{a}_1|} \times \frac{|\mathbf{a}_2| \sqrt{2}}{|\mathbf{a}_2|} \right) R45^\circ = (\sqrt{2} \times \sqrt{2}) R45^\circ.$$

However, the overlayer can also be described in a way without any rotation. In this case, the length of the vectors of the unit cell of the overlayer will be twice the length of the vectors for the substrate. In addition to the corners, this unit cell will also have an oxygen atom at the center. Thus, the Wood's notation become

$$q \left(\frac{|\mathbf{a}_{o1}|}{|\mathbf{a}_{s1}|} \times \frac{|\mathbf{a}_{o2}|}{|\mathbf{a}_{s2}|} \right) R\Omega = c(2 \times 2)$$

$c(2 \times 2)$ is often used instead of $(\sqrt{2} \times \sqrt{2}) R45^\circ$, although, $(\sqrt{2} \times \sqrt{2}) R45^\circ$ is the primitive unit cell. The example above illustrates that an overlayer can be described by the Wood's notation in several ways. One often chose the most convenient unit cell, which is not always the primitive unit cell.

2.5 Oxidization of Cu(100)

Oxygen adsorption on the Cu(100) surface has been extensively studied over the last two decades. Oxygen molecules adsorb onto the surface and spontaneously dissociate in the

process [10, 11]. Three surface phases are observed prior to bulk oxide formation, which occurs when oxygen penetrates the surface and begins to form 3D grains of copper oxide in the bulk of the crystal [12].

Oxygen atoms have been shown to adsorb at the hollow sites of the Cu(100) surface [10, 13]. For temperatures lower than 473 K and coverages up to 0.3 ML^2 , these oxygen adatoms occupy half of the available hollow sites locally, forming an ordered $c(2 \times 2)$ overlayer, as shown in Fig. 2(a). The $c(2 \times 2)$ structure does not form large domains that cover the surface; instead, nanometer-sized domains have been observed separated by zig-zag boundaries of clean Cu(100), with saturation occurring at about 0.3 ML [12]. Above this coverage, the Cu(100) surface itself begins to reconstruct. As indicated in Fig. 2(b), every fourth row of copper atoms in the [010] direction is removed, and a $(2\sqrt{2} \times \sqrt{2})R45^\circ$ structure is formed. This phase is referred to as the missing row (MR) structure. At a coverage of 0.5 ML, the MR structure covers the entire surface. It should be noted that the MR and the $c(2 \times 2)$ have the same amount of oxygen atom per unit cell, the MR is simply the $c(2 \times 2)$, but every fourth diagonal row is missing [14, 15, 16]. The driving force for the formation of the MR structure can be explained by stress relief. It has been shown that the adsorption of oxygen induces a compressive surface stress, which increases with oxygen coverage. Eventually, removal of a row of Cu atoms to form the MR structure becomes favorable and gives a stress relief [10, 17].

Because of the square symmetry of the Cu(100) surface, the MR structure can form with two different orientations, one where the missing rows align along the [010] direction and one where the missing rows align along the [001] direction. As these domains are symmetrically equivalent, both are expected to form in equal proportions on the surface. The presence of these domains makes the MR easy to identify in STM images, as will be shown in Section 5.1.

The copper atoms that are removed when the MR is formed nucleate on the terraces, to form islands, or at the step edges, and exhibit the same MR structure as the rest of the surface. Upon exposure to much higher quantities of oxygen, these islands and step edges act as nucleation sites for growth of bulk-like Cu_2O islands [18]. The Cu_2O islands start to grow into the subsurface before it has covered the whole surface [18].

Surface X-ray diffraction experiments performed by H. Iddir, et. al, showed that when the MR structure is heated to above approximately 473 K a transition to a disordered $c(2 \times 2)$ structure is observed. This observation was explained as a disordering of the Cu atoms in the topmost layer such that a structure is formed which has 25% Cu vacancies randomly distributed (note that the MR structure can be considered as a structure made up of 25% Cu vacancies in an ordered arrangement). When the surface is cooled down below 473 K, the MR forms again [19].

²Monolayer (ML) is defined to be the number of copper surface atoms, e.g. an oxygen coverage of 0.5 ML have half as many oxygen atoms as the clean copper surface have copper atoms

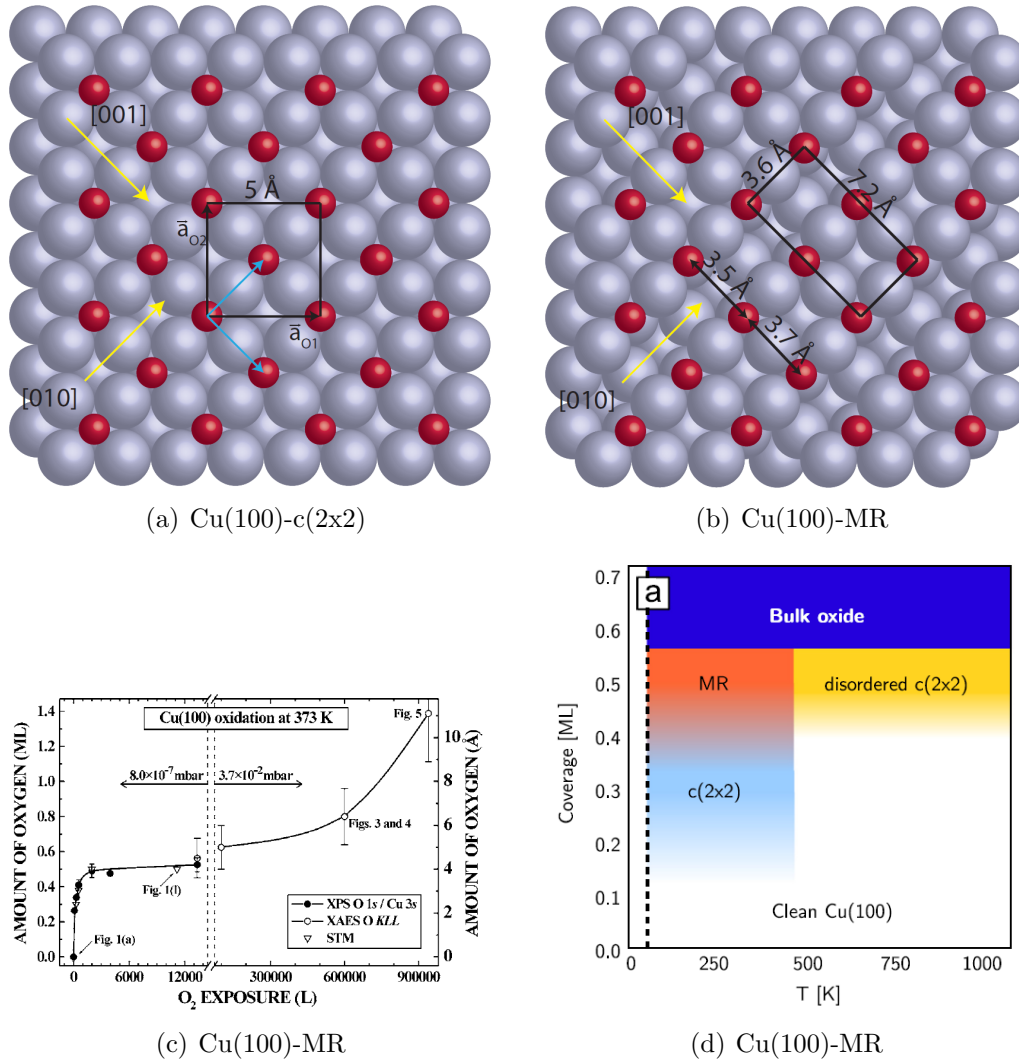


Figure 2: (a),(b) Structures formed by oxygen on Cu(100), (c) oxygen coverage on Cu(100) measured as a function of O₂ exposure, as determined by various techniques, and (d) phase diagram showing the structures observed at various coverages and temperatures. The gray spheres in (a) and (b) are the copper atoms and the red spheres the oxygen atoms. The yellow arrows indicate the [010] and [001] directions. (a) The c(2x2) structure formed for coverages below 0.3 ML, where oxygen atoms adsorb above hollow sites. The centered unit cell is shown as a square with its size indicated. The unit cell vectors are shown as black arrows. The blue arrows show the vectors of the primitive $(\sqrt{2} \times \sqrt{2})R45^\circ$ unit cell. (b) The missing row structure formed at coverages between 0.3 and 0.5 ML. The unit cell is shown as a rectangle with its length and width indicated. The distance between the oxygen atoms alternates between 3.5 Å and 3.7 Å along the [001] direction due to relaxation in the direction of the missing Cu row. (c) Bulk Cu₂O is observed for coverages above 0.55 ML. Both (c) and (d) are reproduced from reference [12].

The MR structure is relatively inert to oxygen uptake once a coverage of 0.5 ML is reached. This is seen in Figure 2(c) where oxygen coverage has been measured by Lahtonen et al. using X-ray photoelectron spectroscopy as a function of O₂ exposure. The coverage increases quickly until approximately 1500 L³ where the curve flattens out.

³Langmuir (L) is defined as 10^{-6} Torr \times 1 second, $1 \text{ L} = 10^{-6}$ Torr/s

Cu_2O is first formed at much higher total exposures [12]. Thus, the MR is a very stable phase under these conditions.

It should be noted that the oxygen atoms in the MR structure and the $c(2 \times 2)$ structure are different. In the $c(2 \times 2)$ structure, the oxygen atoms have four adjacent copper atoms in the surface plane. In contrast the MR the oxygen atoms have only three adjacent copper atoms in the surface plane. However, the distance between the oxygen atoms and the second copper layer is also different between the two structures. The oxygen in both structures is positioned above a copper atom in the second copper layer. The distance between the copper atom and the oxygen atom in the MR is $\sim 2 \text{ \AA}$, while for the $c(2 \times 2)$ it is $\sim 2.5 \text{ \AA}$ [14, 20]. Thus, the chemical environment of the oxygen atoms is different between two structures. This manifests itself in X-ray photoelectron spectroscopy experiments; see the corresponding part in the method section for a more detailed description. The core electron binding energies are different between the $c(2 \times 2)$ and MR structure. This has been shown by Tillborg, *et. al.*, who have done XPS measurements on the system at different coverages [21]. The result can be seen in Figure 3. The experiment was done by dosing oxygen in steps such that oxygen coverages of 0.13, 0.23, 0.34, 0.47 and 0.5 ML was measured. In between each exposure, an XPS measurement was done for the O 1s peak. The temperature while dosing was 500 K and at the measurement 300 K. Although, the temperature for the exposure will give a disordered $c(2 \times 2)$ structure for high enough coverage, and no ordered structure for low coverage, the measurement was done at 300 K which gives an ordered $c(2 \times 2)$ at low coverage and MR at 0.5 ML. Therefore, the measured XPS comes from either the $c(2 \times 2)$ or the MR.

It can be seen from Figure 3 that at a coverage of 0.13 ML the O 1s peak is at 529.5 eV. The peak has a slight shift towards higher binding energy, 529.6 eV at a coverage of 0.23 ML. At a coverage of 0.34 ML the O 1s peak is at 529.8 eV. At the higher coverage, 0.47 ML and 0.50 ML, the peak has shifted to 530.1 eV. As mentioned before, at a coverage lower than 0.3 ML only the $c(2 \times 2)$ structure is observed. Therefore, it can be concluded that the peak at $\sim 529.6 \text{ eV}$ comes from the $c(2 \times 2)$. However, at 0.5 ML only the MR exist, therefore, the O 1s peak at $\sim 530.1 \text{ eV}$ originates from the oxygen in the MR structure. The resolution is not sufficient to resolve the two peaks. Therefore, one only sees one peak that shifts continuously with the increasing coverage.

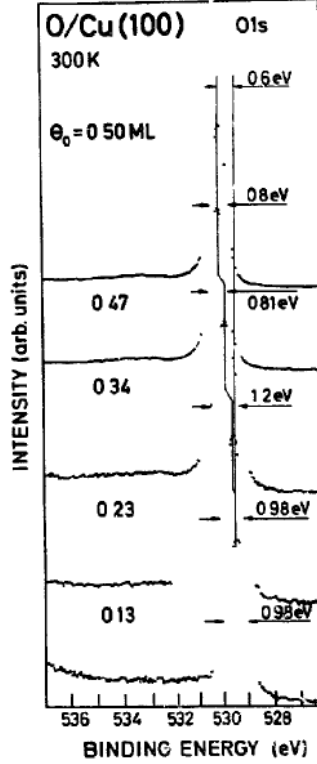


Figure 3: O1s XPS spectra obtained for various oxygen coverages on Cu(100). The vertical lines indicate the peak position. The peak shifts from 529.5 eV at low coverage to 530.1 eV at high coverage. The FWHM is indicated by the arrows. The experiment was performed by exposing the Cu(100) surface to O₂ in steps at 500 K, then cooling the sample down to 300 K for the measurement. The figure is reproduced from reference [21]

The reciprocal lattice of the $c(2 \times 2)$ structure is best described in terms of its primitive $(\sqrt{2} \times \sqrt{2})R45^\circ$ unit cell. As the square overlayer unit cell is formed by rotation of the substrate basis by 45° and expansion by a factor of $\sqrt{2}$, the corresponding reciprocal lattice can be constructed by 45° rotation of the substrate lattice and a *contraction* by a factor of $\sqrt{2}$, as seen in Figure 4(a). The coordinates of reciprocal space are defined by the reciprocal lattice of the substrate (see Figure 1(c)). It can be seen in Figure 4(a) that the reciprocal lattice points of the substrate and the overlayer will coincide when k and h are integers. The $(\sqrt{2} \times \sqrt{2})R45^\circ$ structure also have reciprocal lattice points at the coordinates $(\pm 0.5 \pm 0.5)$.

Formation of the MR structure results in a doubling of the periodicity of the $c(2 \times 2)$ structure in one direction. This means that the reciprocal unit cell of the MR will be the same as the $c(2 \times 2)$ structure in one direction but half the length in the other direction; see Figure 4(b). It can be seen from the figure that half of the reflexes due to the MR structure coincide with those from the $c(2 \times 2)$ structure, while half do not.

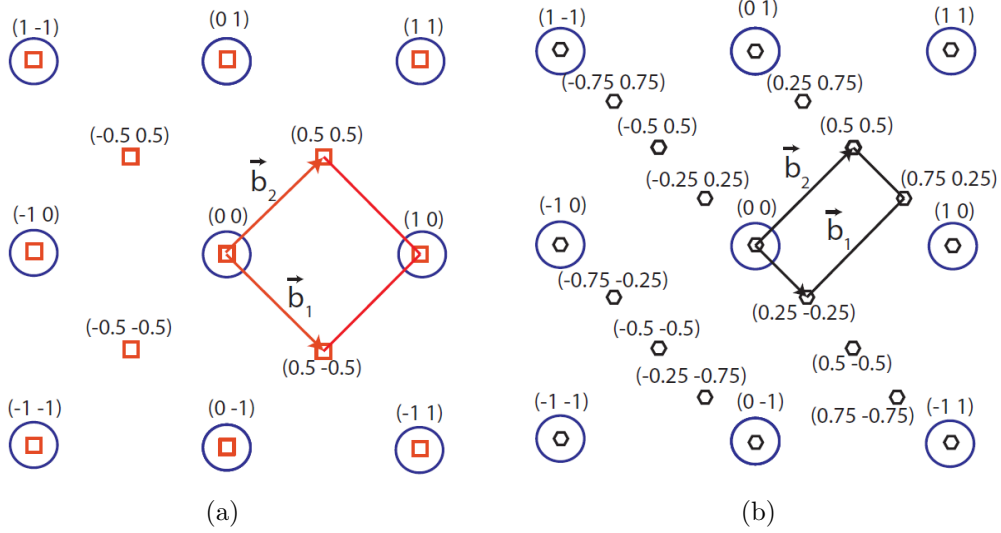


Figure 4: The reciprocal lattices of the (a) $c(2 \times 2)$ and (b) MR structures. In (a) the red arrows and square correspond to the reciprocal lattice vectors and the unit cell, respectively. In (b) these are indicated in black. The coordinates of the reciprocal lattice points defined with respect to the substrate reciprocal lattice, which is shown as blue circles.

3 Method

In this section, the experimental methods and equipment that have been used in the study will be explained and discussed.

3.1 Low-Energy Electron Diffraction

Low-Energy Electron Diffraction (LEED) is a relatively easy method for a quick qualitative determination of the structures of surfaces. LEED makes use of the fact that electrons, like all particles, exhibit wavelike diffraction effects. The wavelengths of the electrons in the low energy range, i.e. 20-300 eV, are of the same order as the distances between atoms, meaning that the electrons can diffract measurably if the atoms are arranged periodically. The low energy electrons also have short inelastic mean free paths, around 5 to 20 Å so that elastically scattered electrons will come from the first few atomic layers of the surface, rather than from the bulk [7].

The surface sensitivity and the relative simplicity of LEED make it an excellent method for this project. It is, for example, fast and easy to determine if the sample has an overlayer structure or if it is clean. LEED was generally used check what state the surface is in before beginning more difficult and time-consuming XPS or STM measurements.

Figure 5 illustrates the basic principle of LEED. The electrons are incident perpendicular to the surface and are scattered by rows of atoms. Constructive interference occurs if the path difference for electrons scattered by different rows is equal to an integer number of the electron wavelength, λ ⁴. From a simple geometric consideration, it can be seen from Figure 5 that the path difference, PD, is simply

$$PD = d \cdot \sin(\theta),$$

where d is the distance between the rows and θ is the angle between the incoming electrons and the outgoing electrons. Thus, constructive interference occurs when

$$m\lambda = d \cdot \sin(\theta) \Leftrightarrow \sin(\theta) = \frac{m\lambda}{d}. \quad (3)$$

From the above equation, it can be seen that the electrons will constructively interfere at specific scattering angles. It can also be seen that the angle increases with increasing d , and *vice versa*.

⁴The electrons wavelength is simply the Broglie wavelength, i.e. $\lambda=h/p$

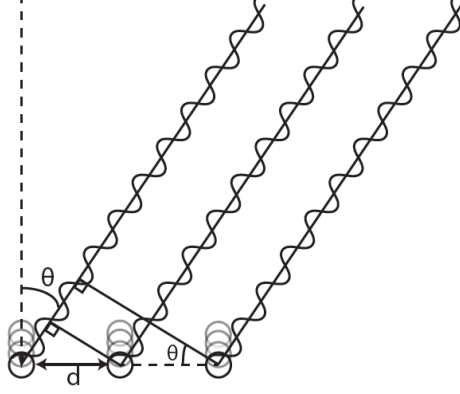


Figure 5: Electrons are scattered by a two dimensional lattice of atoms with a spacing of d between the rows. The dashed line is the incoming electron beam. The black lines and waves are the scattered electrons.

Another way to describe the process is by using wave-vectors, \mathbf{k} , which is a measurement of an electrons momentum [7]. The magnitude of the incoming electrons wave-vectors is equal to

$$|\mathbf{k}_0| = \frac{2\pi}{\lambda}$$

With this equation 3 becomes

$$|\mathbf{k}_0| \cos(\theta) = \frac{2\pi}{d} m \quad (4)$$

The electrons that are considered are only those which scatter elastically. Therefore, the outgoing and incoming electrons wave-vectors will have the same magnitude, i.e. $|\mathbf{k}_0| = |\mathbf{k}_{out}|$. The left-hand side of equation 4 can then be seen as the outgoing electrons wave-vector component parallel to the two-dimensional lattice. The incoming electrons are perpendicular to the surface and, therefore, have no parallel component in its wave-vector. The consequence is then that the left-hand side of equation 4 is the change in the in the parallel component of the wave-vectors, $\Delta\mathbf{k}_{\parallel}$. Thus, the equation becomes

$$|\Delta\mathbf{k}_{\parallel}| = \frac{2\pi}{d} m$$

A hexagonal lattice is considered in Figure 6. The rows that are considered are shown as black dashed lines. It can be seen from the figure that d can be written as

$$d = |\mathbf{a}_1| \cdot \cos(\varphi).$$

Thus, $|\mathbf{k}_0|$ can be written as

$$|\Delta\mathbf{k}_{\parallel}| = \frac{2\pi m}{|\mathbf{a}_1| \cdot \cos(\varphi)} = |\mathbf{b}_1| m.$$

For a square **lattice**, the $\cos(\varphi)$ is equal to 1. The electrons can also scatter in the same way from the red dashed lines in Figure 6. This will give an additional condition for $|\Delta\mathbf{k}_{\parallel}|$

$$|\Delta\mathbf{k}_{\parallel}| = |\mathbf{b}_1| m + |\mathbf{b}_2| n,$$

where n is an integer. It should be noted that $|\mathbf{b}_1|$ and $|\mathbf{b}_2|$ are the length of the unit cell vectors for the reciprocal lattice. Furthermore, it can be shown that for constructive interference to occur the change of \mathbf{k}_{\parallel} has to be equal to a reciprocal lattice vector [7]. Therefore, the condition for constructive interference will become:

$$\Delta\mathbf{k}_{\parallel} = \mathbf{G} = h\mathbf{b}_1 + k\mathbf{b}_2,$$

The pattern of diffracted electrons in LEED corresponds directly to the surface reciprocal lattice.

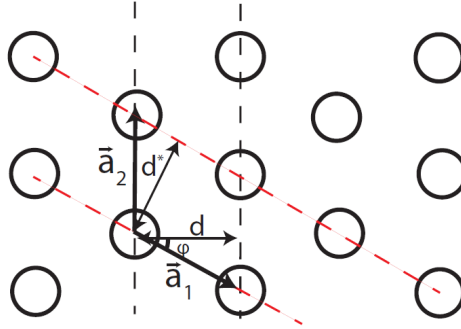


Figure 6: A hexagonal lattice of atoms with unit vectors \mathbf{a}_1 and \mathbf{a}_2 . The rows of atoms that are considered are indicated with dashed lines. d is the distance between the rows of atoms that is considered.

3.1.1 Setup

Figure 7 shows a schematic sketch of the experimental setup of LEED. The first stage consists of an electron gun that creates a monochromatic electron beam with energy E_p . The electron gun is connected to electronics where the filament current can be varied along with the electron kinetic energy and the voltages on electrostatic lenses which focus the beam. The sample is placed in front of the LEED apparatus such that the electron beam will be incident on the sample normal to the surface plane. The sample is grounded so that it does not accumulate charge and thus it is important that the sample is conducting.

After the electrons have scattered elastically they pass through a set of four grids. The first grid, rightmost grid in Figure 7, is grounded so that there is no electric field around the sample which would distort the diffraction pattern. The second and third grids have a voltage applied to them which is slightly less than that corresponding to the electron incident energy, with the purpose of repelling electrons that are scattered inelastically from the surface. The last grid is grounded such that the potential drops down to zero at this point [8].

The detector consists of a fluorescent screen which is biased positively such that the electrons are accelerated towards the screen after passing the energy filter. The acceleration usually is in the range of a few keV, so the electrons have enough energy to create light upon impact which is recorded by a camera and displayed on a computer screen.

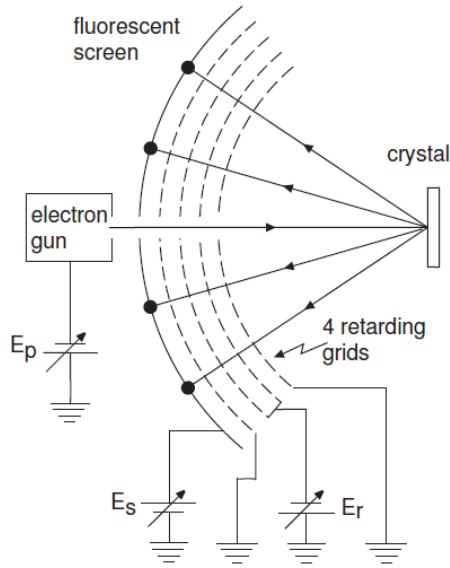


Figure 7: A schematic diagram of the LEED apparatus. E_p denotes the energy of the electrons, which is set by the electron gun. The right going arrow indicates the incoming electron beam and the left going arrows indicates the diffracted electrons. The figure is reproduced from reference [8].

3.2 X-ray Photoelectron Spectroscopy

A common experimental method in surface science is X-ray Photoelectron Spectroscopy (XPS). XPS is used to determine what elements exist on a surface and their chemical state. The basic principle of XPS is the photoelectric effect: photons of sufficiently high energy which strike the surface cause electrons to be emitted whose kinetic energies can be characterized. The electrons have a typical kinetic energy of around 100 eV, giving them an inelastic mean free path of $\sim 10 \text{ \AA}$ [22]. This means that the electrons that are measured will originate from the first few atom layers, making XPS a surface sensitive method. Due to energy conservation, the kinetic energies of the electrons can be related to their binding energies in the material according to:

$$E_{kin} = h\nu - E_{bin} - \Phi$$

or

$$E_{bin} = h\nu - E_{kin} - \Phi \tag{5}$$

where E_{kin} is the kinetic energy of the electron, h Planks constant, ν the frequency of the photon, E_{bin} the binding energy of the electron and Φ the work function [22]. This is illustrated in Figure 8:

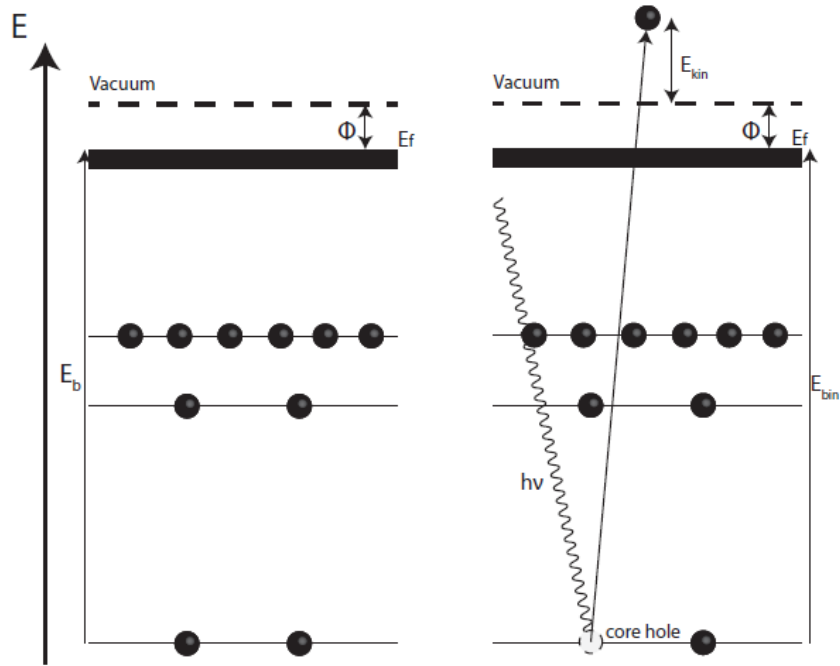


Figure 8: Illustration of the principle of XPS. E_f is the Fermi level.

If the kinetic energy, photon frequency and work function are known the binding energy can be easily calculated from equation 1. However, the work function is not always constant making it impractical to use. Instead, for metal surfaces, the Fermi energy is used as a reference to calibrate the energy scale, as binding energy at the Fermi level is 0 by definition [22]. The Fermi energy can be measured together with each spectrum and used to correct the binding energy. All spectra shown in this thesis have been calibrated in this manner.

In XPS, electrons emitted from core levels are used. One reason for using the core levels is that the binding energies of different elements increase rapidly with increasing atomic number. For example, the difference between the binding energies of the 1s electrons in carbon and oxygen is approximately 240 eV, as will be seen later. Thus, it is simple to distinguish different elements by using photoemission from the core levels [22].

As mentioned above the binding energies of the core electrons reveal what chemical elements are present, but they also provide information about the atoms' chemical environments. Although the core electrons are not directly involved in chemical bonding, a change in chemical environment will produce a change in the potential felt by the electrons in the core levels. Thus, within this "initial state approximation," the binding energies of core electrons are expected to increase or decrease following this changing potential. These small changes in binding energy are referred to as chemical shifts. Although the directions and magnitudes of the chemical shifts observed for various species are also influenced by the energies of the atom's final states, and thus can be difficult to predict based on e.g. relative electronegativity values, they nevertheless often follow regular trends and can in any case be used as fingerprints for different chemical species [22].

Sometimes the electrons can lose energy before they exit the surface. The loss of energy can come from excitation from the valence electrons to unoccupied states at lower binding energies. Such inelastically scattered electrons will appear in the spectra at higher

binding energies. Where single, discrete excitations occur, this will result in distinct peaks in the XPS spectra, whereas electron-hole excitations at the Fermi level of a metal can result in continuous energy loss, causing the peaks to become asymmetric, with a tail extending towards the high binding energy side of the spectrum [23].

3.2.1 Peak shape

The peaks in an XPS spectrum are not infinitely narrow at their respective binding energies but instead have distinct peak shapes with finite widths. The natural line shape of a peak is a Lorentzian whose width corresponds to the lifetime of the core hole created in the photoemission process. The relationship between the lifetime and the line width of the Lorentzian, i.e. the uncertainty in the binding energy, is the Heisenberg uncertainty principle which states that the product of the uncertainty in energy of a state and the state's lifetime is larger than or equal to $\hbar/2$, i.e. $\Delta E \times \tau \geq \hbar/2$. Therefore, the shorter the lifetime of the core hole, the broader the Lorentzian profile and vice versa. It is, therefore, possible to calculate the lifetime of the core hole from the Lorentzian. It should be noted that the width of the Lorentzian is determined by the state the atom is left in under the photoemission process; therefore, the shape of the Lorentzian is expected to be independent of e.g. the specific experimental parameters and the material's temperature [22].

The peaks in an XPS spectrum are further broadened by the energy distribution of the X-ray beam, atomic vibrations in the crystalline structure, the energy resolution of the analyzer, homogeneity of the species measured, etc.. The combination of these effects typically results in a Gaussian distribution added to the peaks' intrinsic shapes. The XPS peaks will, therefore, be a convolution of a Gaussian and a Lorentzian peak, referred to as a Voigt function. Unlike to the Lorentzian, the Gaussian width is expected to change if parameters like temperature or the energy distribution of the X-ray beam change. Thus, the line width of the XPS peaks can be made sharper by adjusting external or internal parameters, e.g. the energy distribution of the X-ray beam and temperature. However, minimizing the width of the energy distribution of the X-ray beam comes at the cost of lower intensity which in some cases can be disadvantageous.

As mentioned above, peaks in an XPS spectrum often exhibit asymmetry, due to excitation of electrons near the Fermi energy [23]. To take this into account, a Doniach-Sunjic (DS) function is used, instead of the Voigt function, to describe the asymmetric peaks. The Doniach-Sunjic function has an extra parameter that determines the asymmetry which if set to zero makes it identical to a Voigt function.

Due mainly to inelastically-scattered photoelectrons emitted from deeper in the crystal, measured XPS peaks for solids generally appear superimposed onto a smooth background. In many cases the background can be approximated locally as a straight line increasing towards higher binding energy.

3.2.2 Experimental Setup

XPS measurements were performed at beamline I311, which was constructed for high-resolution photoemission spectroscopy [24]. The undulator source at this beamline pro-

duced synchrotron light with energies in the range of 30-1500 eV. The desired photon energy was selected by a monochromator.

The end-station consisted of two vacuum chambers connected vertically with each other through a gate-valve. The sample could be transferred between the chambers through a manipulator. The sample was mounted on the manipulator by clamping it with a bent tungsten wire. The temperature was measured using a thermocouple spot welded to the side of the crystal. The manipulator allowed translation in the x, y and z-directions as well as rotation about the vertical axis. This manipulator allowed cooling of the sample with liquid nitrogen to temperatures as low as 100 K.

The upper vacuum chamber served as a preparation chamber where the sample could be cleaned by sputtering and annealing cycles. The sputtering was done using a sputter gun providing an argon ion beam with variable energy and intensity. The sample was heated by running a current through the tungsten wires that held the sample. The preparation chamber was also equipped with a LEED apparatus so the state of the surface could be checked. The chamber was also equipped with several valves allowing various gases to be dosed into the chamber. XPS spectra were measured in the lower chamber, which was equipped with a hemispherical electron energy analyzer.

3.2.3 Data analysis

XPS spectra were analyzed using the program Fitxps v.2.12 written by David L. Adams. Spectra were fits using combinations of DS functions with linear or parabolic backgrounds. The program fits the peaks by minimizing the sum of the squares of the residuals between the data and the peaks. For every peak five parameters could be fitted: energy, height, the full width at half-maximum (FWHM) of the Lorentzian component, the FWHM of the Gaussian, and an asymmetry parameter alpha. It was possible to either fix the parameters or let them vary within a specific range. It was also possible to impose correlations between parameters corresponding to different peaks. For example, the FWHM of the Lorentzians were usually fixed to each other, unless something else was expected.

After the fit is done, FitXPS provides the parameters of the fitted peaks, their summed intensity, and the fitted background function. The background was subtracted from the spectra for plotting in this thesis. Because the cross section for photoexcitation tends to be approximately the same for an element independent of its chemical environment [22], it is possible to estimate the relative amounts of different species on the surface by taking the ratio between the peaks, assuming diffraction and attenuation effects are negligible. For example, the relative coverages of adsorbed CO and CO₂ on a surface can be estimated as the ratio between the C 1s peaks of CO and CO₂.

Determination of absolute coverages of surface species directly from absolute signal intensities is more difficult, as the signal intensities are affected by e.g. the intensity of the X-ray beam, which can be highly variable. However, using a surface structure with a known composition as a calibration standard, it is possible to estimate such absolute coverages in some cases. For example, in the present study it is known that the MR structure contains 0.5 ML of oxygen, so that the oxygen coverage for a partially-reduced surface can be determined from the area ratio of the O1s peak with that from the pristine MR.

3.3 Auger Electron Spectroscopy

After photoionization, as illustrated in Figure 8, an ion is left in an excited state, with a hole in the ionized core level. The ion can be deexcited to a lower-energy state by an electronic transition from a level with lower binding energy. The energy released in this process takes the form of either an emitted photon (X-ray fluorescence) or a secondary electron which escapes to the vacuum with the kinetic energy of E_{kin} . The emission of such electrons is known as the Auger effect, named for Pierre Auger, who discovered the phenomenon. Although the kinetic energy of the Auger electrons can be relatively large, up to ~ 1000 eV for Cu, the inelastic mean free path is still small, around ~ 20 Å[8]. Thus, the signal originates from the surface vicinity, making AES a surface sensitive method. The X-ray fluorescence (left) and Auger electron (right) process are illustrated schematically in Figure 9. In Auger Electron Spectroscopy (AES) the kinetic energies of emitted Auger electrons are used to determine the chemical composition of the surface [22].

The kinetic energy of an Auger electron is estimated by the equation [7, 22]

$$E_{kin} = E_A - E_B - E_C - \Phi, \quad (6)$$

where E_A is the energy level of the core hole, E_B the binding energy of the electron filling the core hole, E_C the binding energy of the shell from which the Auger electron is emitted, and Φ is the work function. Particular Auger emission processes are denoted by the three electron levels involved in the process. For example, Auger emission from an oxygen atom through ionization of the 1s orbital (K shell), filling of the core hole by decay from the 2s (L_1) shell and emission from a 2p (L_2 or L_3) shell would be denoted $KL_1L_{2,3}$, or often simply KLL.

From eq. 6, it can be seen that E_{kin} is determined solely by the electronic levels in the ionized atom; there is no term in the equation related to e.g. the process which created the core hole such as the incoming photon energy or electron energy. The kinetic energies of the Auger electrons that are measured are only determined by the electronic structure of the ionized atom. Therefore, the spectrum of Auger electrons in kinetic energy is characteristic for each element and can be used for elemental analysis of surfaces.

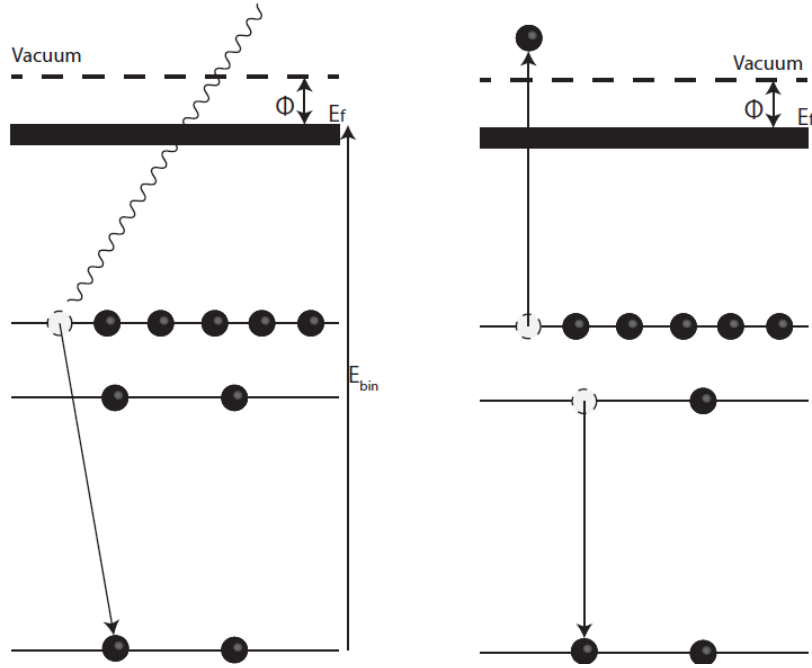


Figure 9: Deexcitation processes for atoms with ionized core levels. Left: X-ray fluorescence. Right: Auger electron emission.

Most of the electrons that are emitted from a solid have lost energy from excitation of interband transitions and plasmons. These secondary electrons produce a large background signal which increases with kinetic energy. The Auger peaks themselves are superimposed on this background signal, making the identification of the peaks difficult. To increase the signal to noise ratio, the derivative of the intensity with respect to kinetic energy, $dN(E)/dE$, is measured instead. The relatively smooth background is then flattened, making the peaks easier to identify. Quantification in this case is based on the difference between the maximum and minimum appearing in $dN(E)/dE$ to the left and right of each Auger peak, which is proportional to the area under the peak, provided the peak shapes do not change drastically [7, 22].

3.3.1 Setup

The Auger electron spectrometer used in these experiments employs a monochromatic electron beam to create the initial core hole excitation. The integrated electron gun produces an electron beam with a typical energy of a few keV, focused to a diameter of 0.1 mm at the sample surface. The electrons which are emitted are then analyzed with a cylindrical mirror analyzer (CMA) coaxial with the electron beam. This analyzer consists of two coaxial cylinders with a voltage applied between them which act as a band-pass filter, allowing electrons within a narrow energy window to reach the detector located opposite the sample. Differential Auger spectra are acquired by applying a small AC component to the voltage between the coaxial cylinders and passing this modulation signal together with the output from the electron detector, a channel electron multiplier, to a lock-in amplifier.

For proper focusing of the electrons passing through the CMA, and hence accurate analysis of their energies, the sample must be precisely aligned before measurement. This

is done by looking at the peak created by elastically scattered electrons. The energy of the electron beam is set by the user and therefore the position of the elastic peak is known. The distance between the detector and the sample is adjusted such that the elastic peak is at E_p .

3.4 Scanning Tunneling Microscopy

Scanning tunneling microscopy (STM) is an imaging method with spatial resolution in the sub-Ångstrom regime. It allows characterization of surface structures at the atomic level. The STM was invented by Binnig and Rohrer in 1981, for which they received the Noble Prize in physics in 1986. Today it is a well-used microscopy tool in surface science [25].

The principle of STM, like all scanning probe microscopy techniques, is that a sharp tip is scanned across the surface, and the interaction between the tip and the surface is measured. In the case of STM, a voltage is applied between the tip and surface, generating a tunneling current when the two are in close vicinity. This tunneling current has a strong dependence on the distance between the tip and the surface, making it possible to measure topology of the surface with atomic-scale precision.

3.4.1 Theory

To get an understanding of the contrast mechanism in STM, the simplest model of the tunneling current can be considered. This can be seen in Figure 10 which illustrates 1D tunneling through a square barrier. The potential, $V(z)$, has a value of V_0 between $z = 0$ and d , but is zero otherwise. This one-dimensional picture of the STM can be used to derive a first approximation of the contrast of the STM images. In quantum mechanics, the electrons are described as wave-function, $\Psi(t, \bar{z})$, that solve the Schrodinger equation. The electron is assumed to be free, which is a good approximation for electrons in metals, and have an energy E [25]. Because the potential that is considered has no time dependence, the wave-function can be factored into

$$\Psi(t, \bar{z}) = e^{-i\frac{Et}{\hbar}} \psi(\bar{z}),$$

where the spatial part of the wave function can be derived by solving the time-independent Schrodinger equation

$$\frac{\hbar^2}{2m} \frac{\partial^2}{\partial z^2} \psi(z) = (V(Z) - E) \psi(z). \quad (7)$$

The problem can be approached by solving the time-independent Schrodinger equation separately for the three regions (1), (2) and (3) (see Figure 10) and then applying boundary conditions. An ansatz is made such that $\psi(z)$ is proportional to its own spatial derivative: $\psi(z) = e^{ikz}$, and this is inserted into the equation 7:

$$\frac{\hbar^2}{2m} i^2 k^2 e^{ikz} = (V(Z) - E) e^{ikz} \Leftrightarrow -\frac{\hbar^2}{2m} i^2 k^2 = (V(Z) - E),$$

which can be rewritten to

$$k = \sqrt{\frac{2m}{\hbar^2}(E - V(Z))}.$$

For the regions (1) and (3) the potential is $V=0$ and therefore k is real, so that ψ takes the form of an oscillating wave:

$$\psi = e^{ikz}, k = \sqrt{\frac{2mE}{\hbar^2}}.$$

In region (2), however, the potential is V_0 , which is greater than the electron energy. This implies that k is imaginary, and can be written in the form

$$k = i\sqrt{\frac{2m}{\hbar^2}(V_0 - E)} = i\kappa$$

This produces a wave-function which decays exponentially in region (2):

$$\psi = \psi(0)e^{-\kappa z}.$$

Classically, the electron would have zero probability to be found in region (2), and certainly could not pass to region (3). The electrons in the quantum mechanical picture, however, have a finite chance to be found in region (2) and (3), allowing it to penetrate the classically forbidden region. This phenomenon, called tunneling, gives STM its name.

The transmission probability, T , which determines the tunneling current, is equal to the ratio of $\psi(z)$ at $z=0$ and $z=d$. This is proportional to:

$$T \propto e^{-2\kappa d}.$$

The transmission probability decays exponentially and, in turn, so does the tunneling current [25]. For a typical barrier height of 4.5 eV, the value of κ is $\sim 10 \text{ nm}^{-1}$, so that the tunneling current drops by a factor of 10 for each 1 Å increase in distance. At equilibrium, electron transfer occurs in both directions and there will not be any net current. However, if a bias potential is applied between the tip and the sample, a finite tunneling current will flow. If the sample is biased positively it will be energetically favorable for electrons to tunnel from the tip into empty states in the sample. If the sample is biased negatively, electrons will instead tunnel from the sample to the STM tip [25].

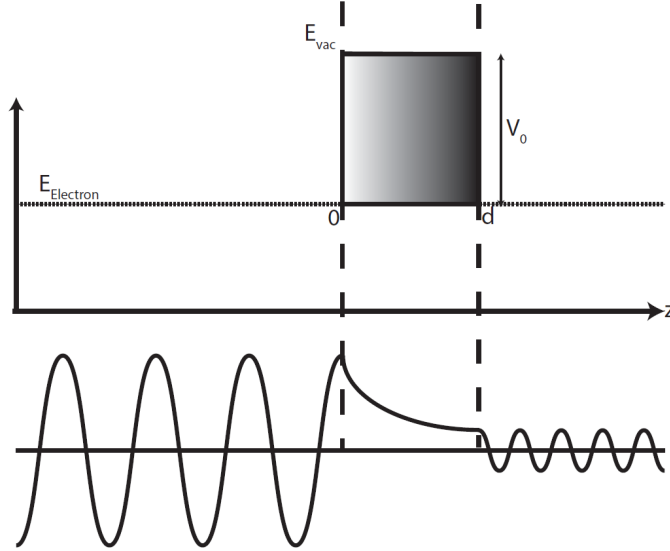


Figure 10: A schematic illustration of the tunneling concept. The gray area is the classically forbidden region while the left is the sample and the right the tip. Below the energy diagram the real part of the wave-function is seen. The wave-function of the electron decays exponentially outside the surface.

The STM can be operated in two modes: constant current and constant height. In the constant height mode, the tip is kept at the same z -position and the tip is scanned in the xy -plane while the current is measured. In constant current mode, the current is kept constant using a feedback loop. The current is set to a specific value, I_0 , and if the current increases the feedback loop will respond by retracting the tip such that the current decrease to I_0 . If the current decreases below I_0 , the feedback loop will respond, and the tip will approach the surface such that the current increases to I_0 . The height of the tip is recorded through the scan.

The constant current and height modes have different advantages and disadvantages. The constant current mode is slower due to the relatively slow response time of the feedback loop. The constant height mode is faster simply because it measures more directly, without the feedback loop. However, in contrast to constant height mode, the constant current mode has a mechanism which prevents the tip from crashing into the surface. If for example, the surface would be rough with numerous atomic steps the tip would simply crash into the surface for the constant height mode. For the constant current mode, however, the tip is retracted by the feedback loop and the crash is then prevented. Because the goal of this project was to study the structures formed on the surface and not any dynamics, there was no need to scan fast. All STM measurements shown in this thesis were therefore acquired in constant current mode.

The interpretation of the contrast in STM as topological is only a first approximation. It is natural to think that the local density of electronic states, or the surface conductivity, would vary across the surface and that the tunneling current would therefore also vary. Thus, in a more realistic (but still approximate) consideration, the STM contrast is a convolution of topological and electronic contrast, making the interpretation of STM images not always straightforward. The theoretical description of the tunneling current that takes into account electronic effects, the local density of states, was developed

by Tersoff and Hamann [26]. The derivation is beyond the scope of this thesis and the interested reader is referred to their original work or to textbooks on STM [25].

3.4.2 Experimental Setup

In this subsection, a schematic description of the setup of STM is presented. A photograph of the STM used in these experiments is shown in Figure 11. The sample is placed in a holder that keeps it from moving. The tip is mounted on a tip holder which is then fixed to the scanning unit. The tip can easily be removed and replaced if needed. The STM is shielded from vibrations by a hanging spring suspension with eddy current damping.

The scanning unit consists of three orthogonal piezo elements, as seen in Figure 11. A voltage can be applied independently to each elements such that the tip moves in the x, y and z-directions. The entire scanning unit itself can be moved towards the sample and horizontally. The current passes first through two pre-amplifiers, one in the vacuum chamber and one outside it. The signal is then passed to the control unit, which is connected to a computer.

The software used to control the STM measurements is MATRIX v3.2. From the software, the bias between the sample and the tip can be set, along with the current setpoint and other scanning parameters.

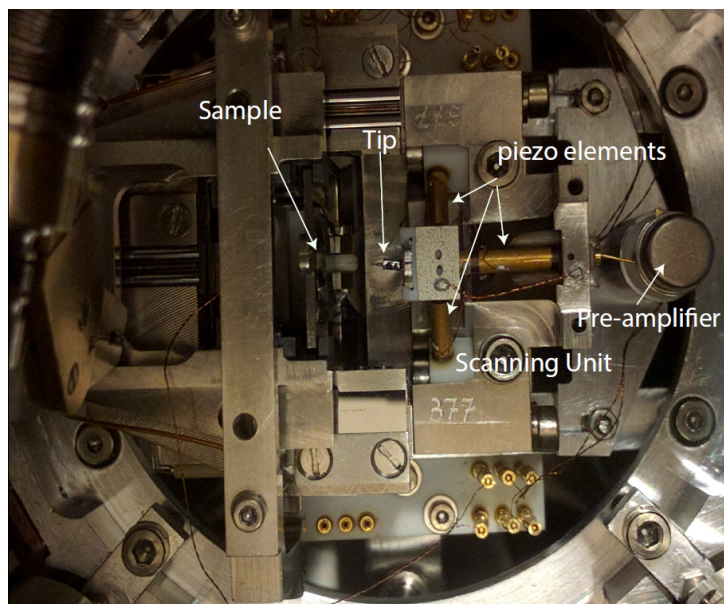


Figure 11: STM setup.

To achieve tunneling conditions, an automated approach mechanism is implemented, controlled by the software. The process starts by first retracting the tip and then moving the scanning unit one step forward. The tip is then extended towards the sample by the z piezo element. If the tunneling current, set by the user, is not obtained the tip is retracted, and the scanning unit takes one step forward. This is repeated until the desired tunneling current is measured.

3.5 STM-chamber

The vacuum system used to perform STM, AES and LEED measurements consists of two chambers, a preparation chamber, and an analysis chamber. This is schematically illustrated in Figure 12. The manipulator in the preparation chamber has a filament underneath the sample for heating by electron bombardment. An Ar ion gun is also mounted on the preparation chamber for sample cleaning by sputtering. Hydrogen and oxygen can be dosed into the preparation chamber through leak valves. The base pressure in the preparation chamber is on the order of 10^{-10} mbar.

Following preparation, the sample can be transferred to the analysis chamber, where the sample can be placed in front of the LEED or AES with a second manipulator. The sample, mounted on its holder, can be moved to the STM with a wobble stick.

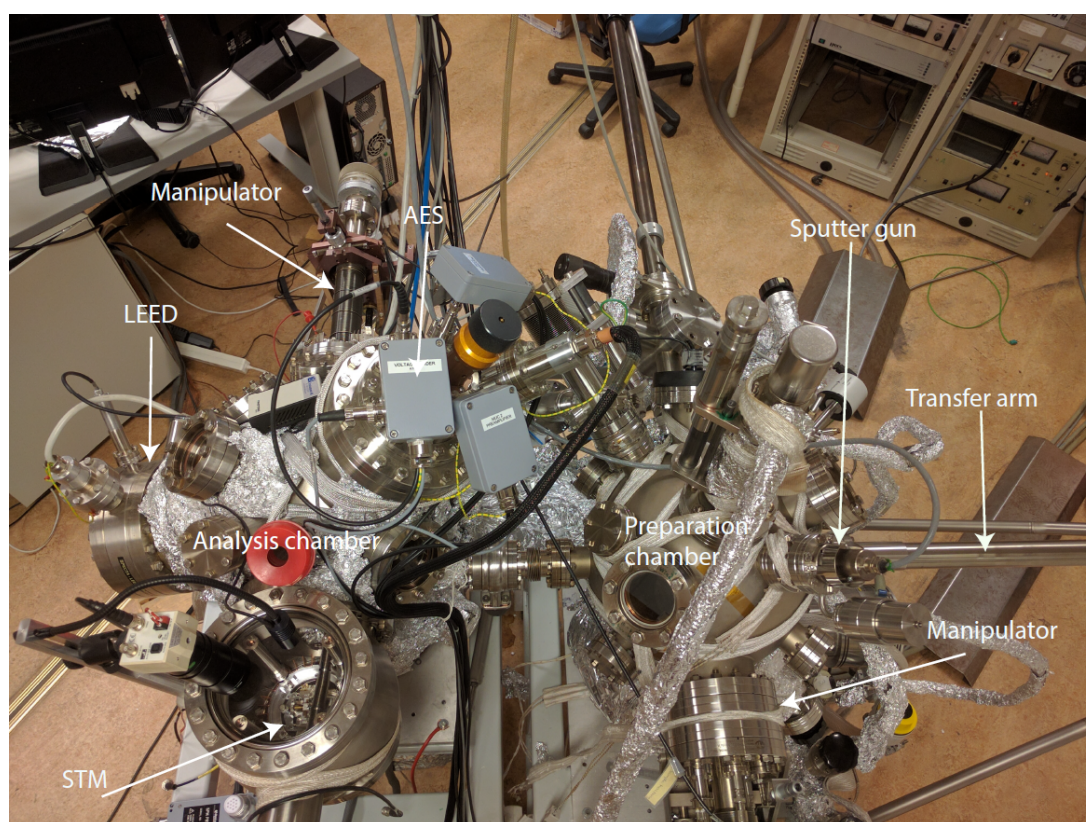


Figure 12: A schematic diagram of the vacuum system used for STM, AES and LEED.

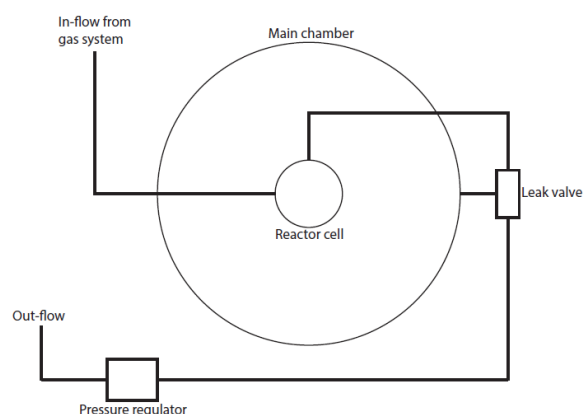
3.6 In-situ flow reactor

In this section the in-situ flow reactor that was used for the reactivity measurement will be discussed. A schematic diagram of the setup is shown in Figure 13(a). The sample is mounted on a heating plate as shown in Figure 13(b), which then is placed in the reactor cell. The sample plate has four screws, two of which are used to secure the sample on the heating plate and two of which are used for heating by passing a current through the plate.

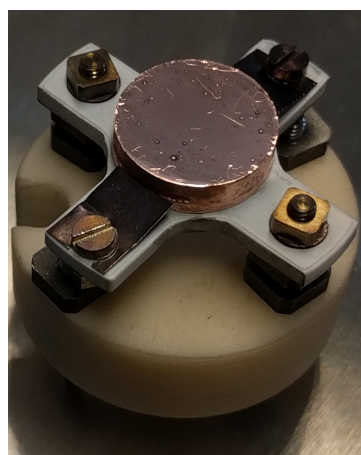
The apparatus consists of two main parts, the reactor cell and the main vacuum

chamber. A residual gas analyzer (RGA or mass spectrometer), a sputter gun, a leak valve for argon, and a turbo-pump are mounted on the main chamber. Two gas lines are connected to the reactor cell for in-flow and out-flow of gasses. The gas flow to the reactor cell is controlled by a separate gas system, not shown in Figure 13(a), which consists mainly of flow controllers which can relegate the gas flow of the different gasses between 0-50 ml/min. The out-flow from the reactor cell is connect to a leak valve, where the gas can be leaked into the main chamber, and then connected to a pressure regulator and a pump.

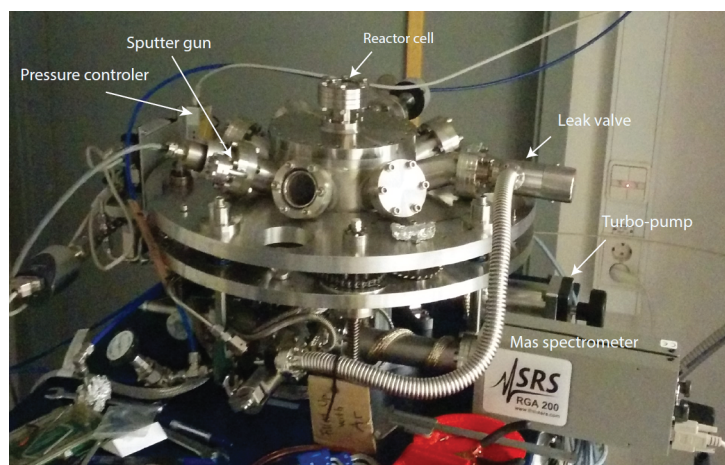
Gas which is leaked into the chamber either through the leak valve or by loosening the seal of the reaction cell is analyzed by the RGA, providing information about the gas composition and thus the catalytic reactivity.



(a) Schematic diagram of the setup



(b) Sample holder



(c) Picture of the setup

Figure 13: (a) A schematic diagram of the reaction cell, (b) a photograph of the sample holder with a Cu(100) crystal mounted, (c) a photograph of the chamber.

4 Experiment

In this section, the experimental procedures will be briefly presented. The results from the experiments will then be presented in the next section.

The aim of the experiments was to characterize the chemical properties of the MR structure, which serves as a model RWGS catalyst. It has been proposed that a combination of oxide sites and metallic sites is necessary, such that CO_2 adsorbs onto the oxide and H_2 onto the metal. Therefore, the differences between the interaction of CO_2 with the MR structure and with the bare Cu(100) surface as well as on a partially-reduced MR surface prepared by exposure to H_2 have been studied. To do this, the MR structure has to be prepared, although the structure is already known, and the reduced MR has to be studied. As a complement to these experiments, tests on the catalytic activity of the Cu(100) surface were conducted, serving as preliminary tests for future in-situ experiments.

4.1 STM, AES and LEED experiments

The sample was mounted on a sample holder made of molybdenum which has a high melting point and is relatively inert to oxidation under the conditions used [12]. Two different Cu(100) crystals were used for the experiments, one 12 mm in diameter and 3 mm thick, the other 8 mm in diameter and 2 mm thick. The temperature was measured with a type-K thermocouple welded to the molybdenum plate next to the sample. This causes an offset in the temperature measurement such that the actual surface temperature is lower than the measured temperature.

The sample was cleaned by cycles of Ar^+ sputtering and annealing. The values for the parameters in the sputtering and annealing cycles are taken from [12]. The sputtering was done with $2 \cdot 10^{-5}$ mbar Ar, 1.5 kV acceleration voltage, and an emission current of 10 mA for 30 min (later the sputtering was done for 15 min). The sample was annealed at 400 °C for 5 min. The LEED pattern was checked, and a sharp 1×1 pattern was observed when the sample was clean.

To prepare the MR structure, the Cu(100) surface was first exposed to $1 \cdot 10^{-6}$ mbar of O_2 for 20 min, i.e. approximately 1200 L, at a temperature of approximately 110 °C. This resulted in a $(\sqrt{2} \times \sqrt{2})R45^\circ$ LEED pattern as expected for the MR structure, and AES showed a clear feature due to adsorbed oxygen. To ensure that saturation of the surface with oxygen was achieved (see Fig. 2(c)), the sample was exposed to the same dose of oxygen a second time. No changes were observed in the relative intensities of the LEED spots or the ratio of oxygen to carbon AES signals, indicating that the treatment was sufficient to produce a surface fully covered by the MR structure. After preparation of the MR structure, it was imaged by STM.

In order to follow the reduction of the MR structure, the sample was exposed to $2 \cdot 10^{-7}$ mbar H_2 at 300 °C for 10 minutes, approximately 100 L, and characterized with LEED, AES and STM. Reduction at several different conditions were tested, but due to poor performance of the STM tip and lack of time, STM characterization of more reduced surfaces was not obtained.

AES measurements were obtained using an incident energy of 3 keV, a beam current of ca. $1.7 \mu\text{A}$, and a periodic modulation of the analyzer pass energy with an amplitude of 3.0 V and a frequency of 9.5 kHz. To correct for creep in the beam current during acquisition of an AES spectrum, the beam current was recorded at points corresponding to the main O and Cu peaks and used for normalization of the intensities.

The AES measurement are mainly used to check the cleanliness of the sample and to estimate the oxygen coverage of the partly reduced surface. The corresponding AES spectrum of the MR structure is shown in Figure 16. The peak at kinetic energy ~ 511 eV is a O KLL peak, and as discussed in section 3.3 the height of the peak corresponds to the number of O atoms on the surface. The intensities of the peaks can, however, vary between different experiments depending on the samples relative position to the channeltron. Therefore, to use the intensities from the peak directly is not appropriate. Instead, the intensity ratio between the O KLL peak and the Cu LMM peak at ~ 918 eV is used instead, and can be used to estimate the coverage on the partly reduced surface. These two peaks are indicated with black lines and arrows in Figure 16.

4.2 XPS experiments

The sample was cleaned in the same manner as for the STM experiments using cycles of Ar sputtering and annealing until no C or O impurities could be detected with XPS. The surface was then oxidized by exposing to O_2 under similar conditions as in the STM lab. Initially, there were problems with surface contamination by carbon during the oxidation process. Contamination was reduced by further degassing of the LEED electron gun and by turning off the pressure gauge during O_2 exposure, but the problem was never completely solved, and all the MR structures characterized showed a small carbon contamination. Each preparation was checked with LEED before any XPS measurements were done.

As in the STM experiments, the reduction of the MR structure was performed by exposure to H_2 at a sample temperature of $300 \text{ }^\circ\text{C}$. Adsorption of CO_2 was performed with the surface at 110 K by dosing CO_2 gas through a leak valve.

After each preparation, XPS measurements covering the C 1s, O 1s and Cu 2p electron levels were performed at liquid nitrogen sample temperature. The photon energies used were 380 eV (C 1s), 620 and 680 eV (O 1s) and 1100 eV (Cu 2p). For each measurement, the Fermi level was measured as well, to use for energy calibration. The O 1s region was measured with both 620 eV and 680 eV photons in order to detect subsurface oxygen, expected to become more intense with increasing photon energy due to the increasing escape depth.

4.3 In-situ flow reaction experiments

The Cu(100) sample was mounted as described in the method section in the flow reactor. The sample temperature could not be measured directly, but approximate temperatures were determined based on a previous calibration against the sample heating current. The surface was sputtered with $8 \cdot 10^{-5}$ mbar Ar, 2 kV and 10 mA for 15 minutes and annealed at $725 \text{ }^\circ\text{C}$ for 5 minutes prior to introduction to the reaction cell.

Prior to reactivity measurements, to remove any oxygen that might have adsorbed during introduction of the sample to the reaction cell (where, upon sealing, the background pressure is not well-controlled), the sample was heated in H₂.

The procedure for the reactivity measurements was as follows: The pressure in the reactor cell was set to 100 mbar by the pressure controller. H₂ was set to flow at a rate of 15 ml/min and the sample was annealed at 550 °C in pure H₂ for 5 min. 15 ml/min of CO₂ was added to the gas flow, such that the sample was exposed to a 1:1 mixture of H₂ and CO₂. The gas was leaked from the reactor cell into the main vacuum chamber and the RGA was set to measure CO, CO₂, H₂O and H₂. The experiment was started when the signals in the mass spectrometer were stabilized. Due to the low conversion rate from CO₂ to CO the flow was stopped for 8-10 minutes, causing formed CO to accumulate in the reaction vessel and increasing the signal. The flow was then started and the temperature was increased by about 10 °C. When the mass spectrometer signal was stable again, the flow was stopped again to check the current activity, and the procedure was repeated until a temperature of 700 °C was reached. In order to make sure that the catalytic effects seen were really related to the sample, the whole experiment was repeated with the Cu crystal removed.

5 Results

The results are divided into three parts. The first covers the creation and reduction of the MR structure, combining results from LEED, AES, STM and XPS experiments. The second part presents the study of CO₂ adsorption on the different surfaces using XPS at the MAX IV Laboratory. Finally, the results of catalytic activity tests using the in-situ flow reactor and mass spectrometer will be presented.

5.1 Formation and partial reduction of the missing row structure

5.1.1 Formation of MR structure

As a starting point, the MR structure, although well-known, had to be prepared and preparation recipes established with LEED, XPS, AES and STM.

The LEED pattern of the clean Cu(100) surface is shown in Figure 14(a). The corresponding square reciprocal lattice, with the unit cell marked blue, is clearly seen. Figure 14(b) shows the LEED pattern after preparing the MR structure by exposing the surface to 1200 L as described in the experiment section. The two domains, rotated 90° with respect to each other, are marked by the red and green rectangles, respectively.

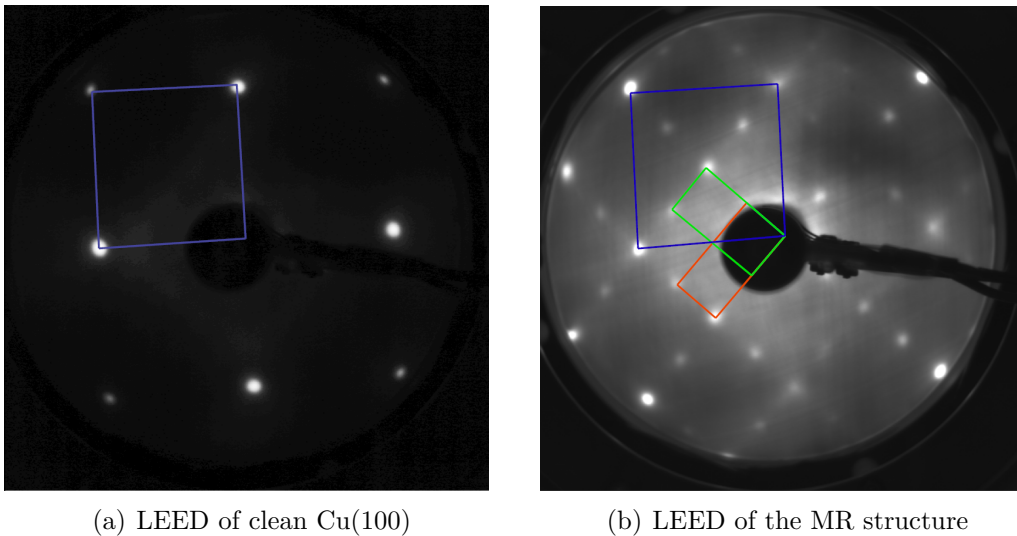
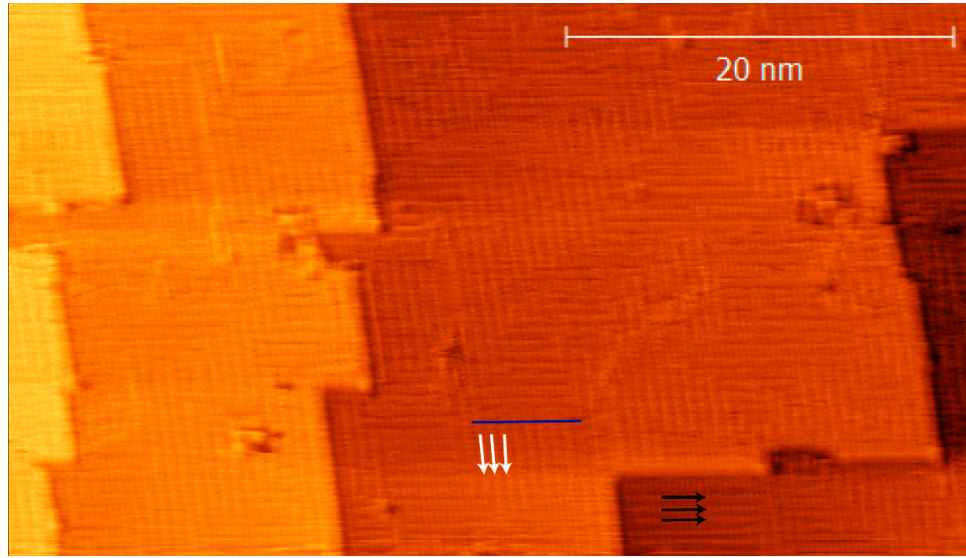


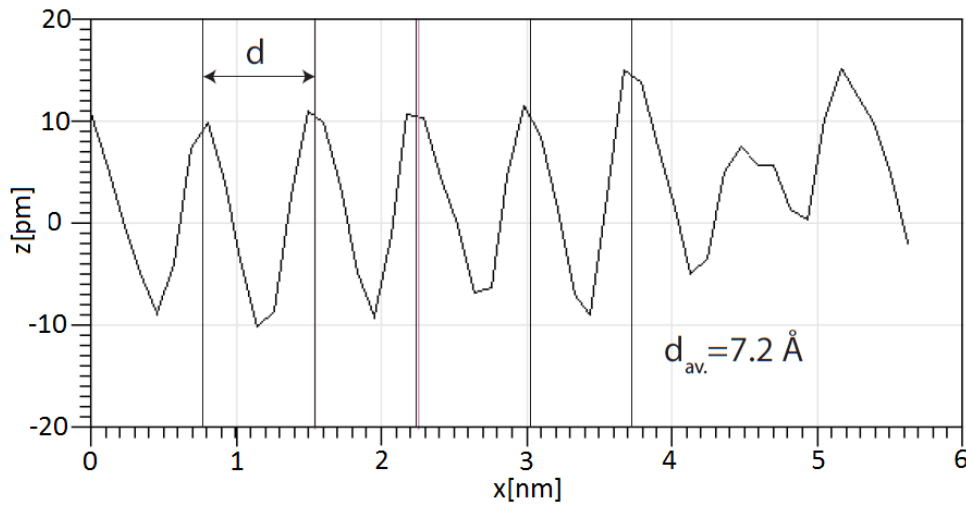
Figure 14: LEED images of (a) clean Cu(100) and (b) Cu(100) with the MR structure. Both images were acquired with an electron energy of 83 eV. The square 1×1 unit cell corresponding to Cu(100) is marked in blue and the two domains of the MR structure are indicated with the red and green rectangles.

An STM image of the MR is shown in Figure 15(a). The surface seems to be covered by a striped structure, with two domains rotated 90° with respect to each other. Figure 15(b) shows a line profile of the height corrugation along the blue line in panel (a). From the line profile it can be seen that the average distance between the bright rows is approximately 7.2 Å, which fits well with the distance of the MRs unit cell in the

direction perpendicular to the missing row, as seen in Figure 2(b). Hence, we conclude that this exposure results in a surface completely covered by the MR structure.



(a)



(b)

Figure 15: (a) STM image of Cu(100) after 1200 L O₂ exposure at 100 °C. (b) Height profile measured along the blue line marked in (a). (a) The two domains in the MR are indicated with white and black arrows. (b) The average distance between the black lines is 7.2 Å.

The corresponding AES spectrum of the surface is shown in Figure 16. The spectrum shows peaks corresponding to O-KLL transitions (main peak at 511 eV) and Cu-LMM transitions (main peak at 918 eV), and no features attributable to other elements. The O:Cu intensity ratio, after correction for the beam current as described in section 4.1 is

$$r_{MR} = \frac{\frac{3.31 \cdot 10^4 - 3.15 \cdot 10^4}{2.22 \mu A}}{\frac{3.58 \cdot 10^4 - 2.39 \cdot 10^4}{2.76 \mu A}} \approx 0.17 \pm 0.005,$$

Considering that the surface is fully covered by the MR structure, this value corresponds

to an oxygen coverage of 0.5 ML, and was used as a calibration for further coverage estimations.

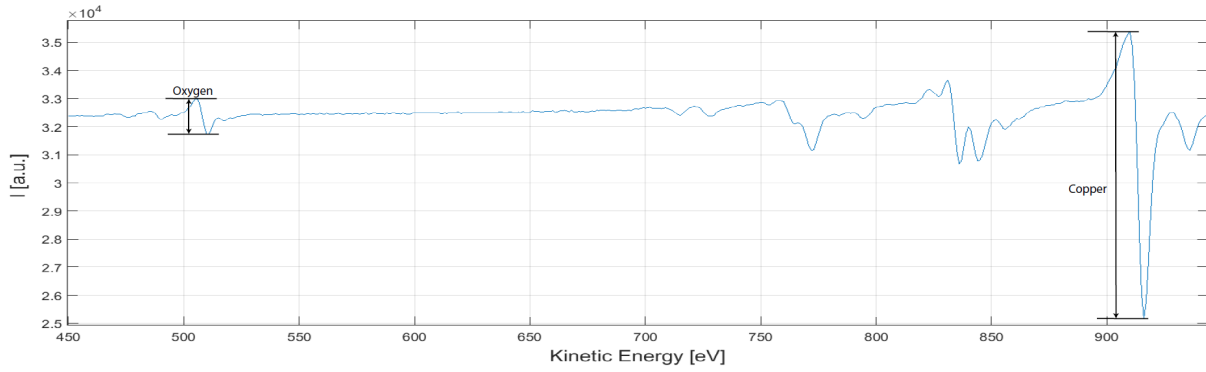


Figure 16: AES spectrum of the Cu(100) surface fully covered by the MR structure. The oxygen and copper peaks that were used for coverage estimation are indicated with black lines and arrows.

An O1s XPS spectrum of the MR structure is shown in Figure 17 together with the result of least-squares peak fitting. In agreement with previous studies, the O atoms in the MR structure give rise to a main peak at 530.0 eV [21]. In addition, there is a broad shake-up peak centered at 533.3 eV [27]. The main O1s peak was fitted with a slightly asymmetric DS profile. The fitting of shake-up peaks is generally hard due to their large width and to the fact that they tend to overlap with the main peak [23, 27]. Here, the shake-up peak is approximated by a broad Gaussian and in subsequent fits its binding energy, intensity, and FWHM were fixed relative to the main O 1s peak.

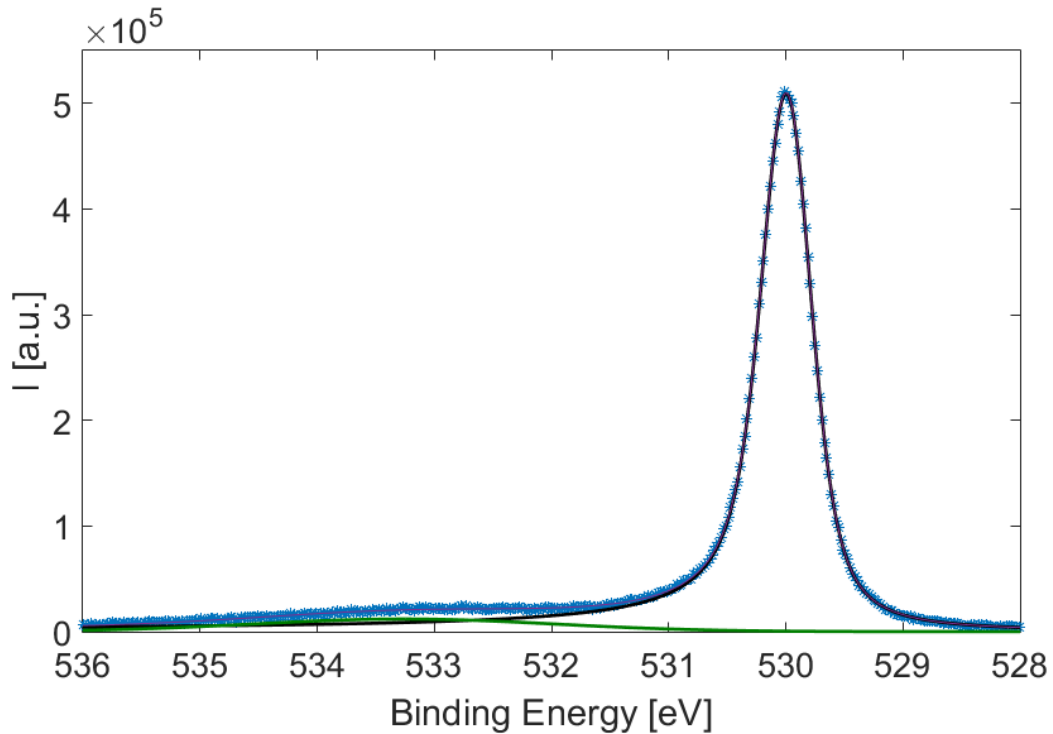


Figure 17: O 1s spectrum of the MR structure. The black line is the main O 1s peak from the MR while the green line is the shake-up peak. The spectrum was measured with a photon energy of 620 eV.

5.1.2 Reduction of the MR structure

After the formation of the MR was established, the reduction of it was studied. O 1s XPS spectra obtained after the MR surface was reduced successively by exposure to increasing amounts of H₂ at 300 °C are shown in Figure 18. It can be seen as the peak is reduced in intensity as the oxygen is removed, it shifts to lower binding energy with exposure and develops a distinct shoulder between ~ 529.0 and 529.5 eV. This behavior is similar to what was observed by Tillborg et al. when measuring the O1s peak as the oxygen coverage was increased, as shown in Figure 3. Initially, for a low coverage (0.23 ML) where the surface exhibited a $c(2 \times 2)$ LEED pattern, they observed the O1s peak at 529.6 eV. With increasing coverage and transformation to the $2\sqrt{2} \times \sqrt{2}$ structure. The observation of a shift to lower binding energy with decreasing coverage is here interpreted as a sign that reduction of the MR structure causes oxygen to adopt a similar bonding configuration as in the $c(2 \times 2)$ structure. No additional spots were observed in the LEED pattern after the reduction, though the spots were slightly broadened and the background became more intense, indicating that the surface became less well ordered. Identification of a $c(2 \times 2)$ phase-if present-is hindered by the overlap of reflexes with those of the MR structure.

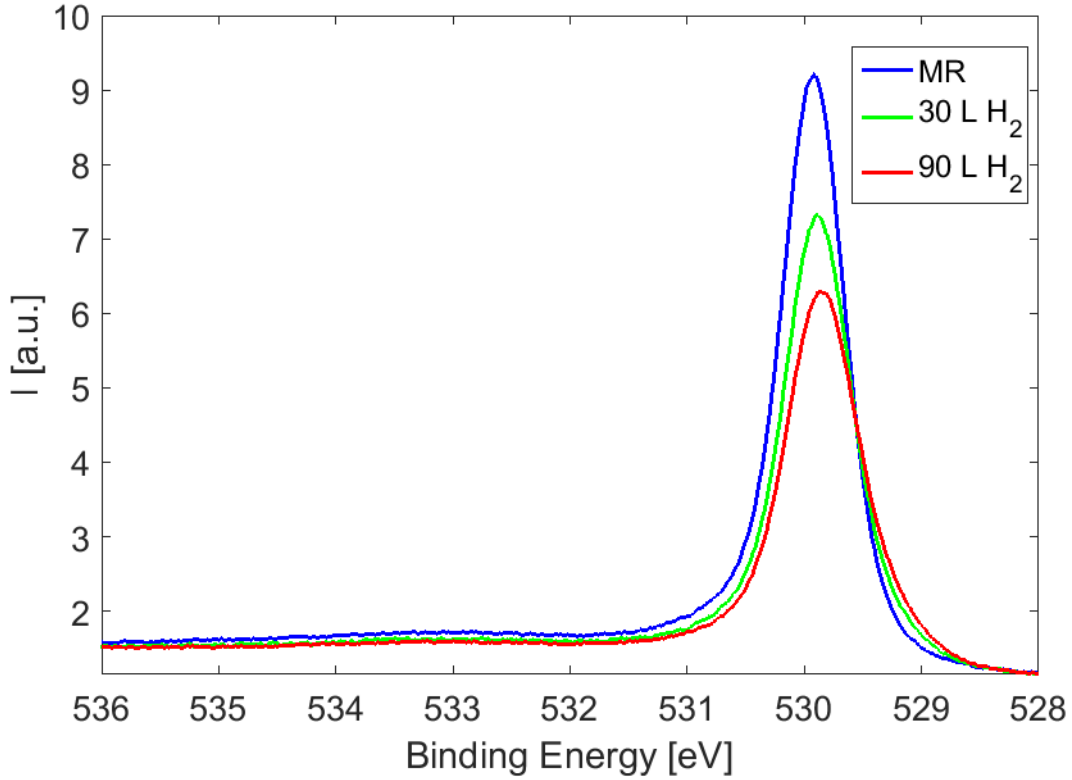


Figure 18: O 1s spectra for the MR structure following successive reduction treatments in H_2 .

The O1s XPS spectrum of the MR structure after reduction by 90 L H_2 is plotted in Fig. 19 together with the result of least squares fitting. The spectrum is well fitted by a combination of a component at 530.0 eV corresponding to that of the pristine MR structure with a new component at 529.7 eV, accounting for the shoulder observed in Fig. 18. This new peak can be attributed to a new oxygen species on the surface. The relative intensity between the peaks at 530.0 and 529.7 eV is the same in measurements acquired using photon energies of 620 eV and 680 eV, indicating that both peaks originate from oxygen located at the surface. Previous studies have reported that subsurface oxygen gives rise to peaks at higher binding energies relative to that of the MR [28], further supporting this interpretation.

To estimate the local oxygen coverage of the reduced regions the peaks in Figures 17 and 19 are compared. The summed intensity of both peaks in Fig. 19 is 40% smaller than the intensity of the peak in Fig. 17. By knowing that the oxygen coverage of a surface fully covered by the MR is 0.5 ML, it can be concluded that the overall oxygen coverage of the partly reduced surface is 0.3 ML. However, the peak from the MR in Fig. 19 is approximately 60% smaller than the MR peak from Fig. 17. This means that the surface is covered by 60% with the reduced phase and the rest of the surface is covered with the MR. For an overall oxygen coverage of 0.3 ML to add up the oxygen coverage of the reduced parts have to be

$$\frac{0.3\text{ML} - 0.4 \cdot 0.5\text{ML}}{0.6} \approx 0.17\text{ML}$$

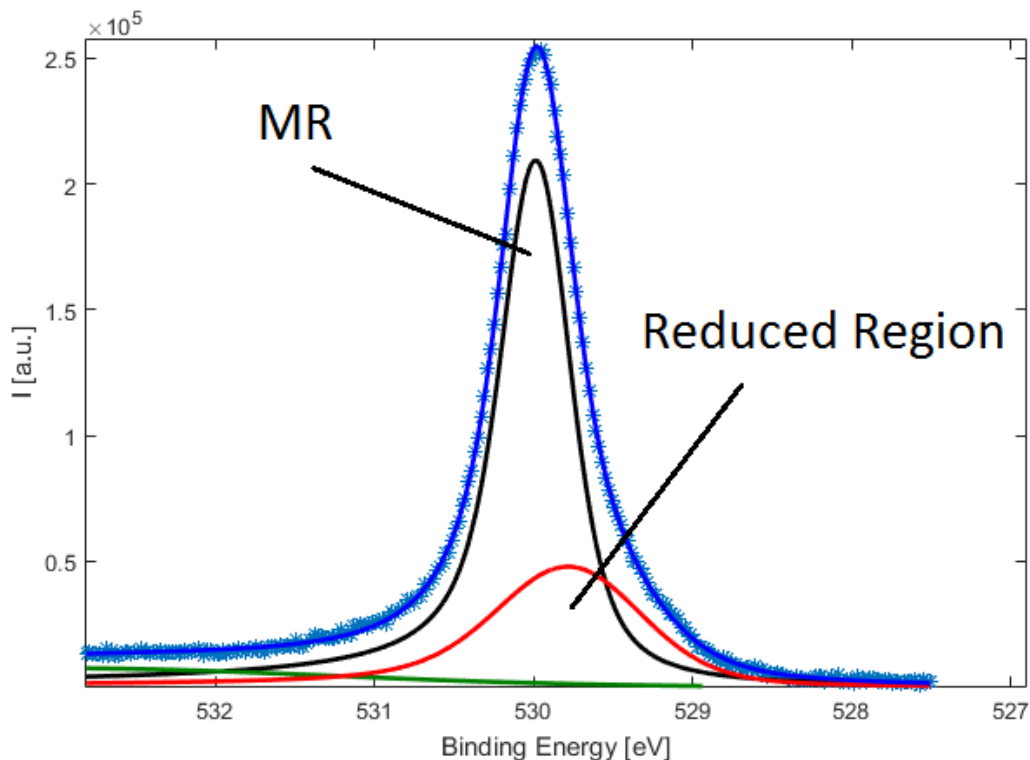


Figure 19: O 1s XPS spectrum showing the results of least squares fitting of the MR structure reduced by 90 L H₂. The peak associated with the MR is black while the peak associated with the reduced regions is red. The spectra are normalized to the background. The spectra were measured with a photon energy of 620 eV.

STM images of a partly reduced surface are shown in Figures 20 and 21. Most of the surface consists of flat terraces covered in the MR structure, as is evident from the visible stripes seen in Fig. 20(b) and 21. A new phase is also apparent in the images, forming on the lower terraces adjacent to step edges (arrows in Fig. 20(a)) and around defects in the terraces. Based on comparison with the XPS and AES data, we assign this new phase to a reduced structure which has been depleted of oxygen. The structure of this new phase is unclear. As can be seen in the high-resolution STM images shown as an inset to 20(b), and in Fig. 21, the structure does not seem to correspond to the $c(2 \times 2)$ phase, was suggested by XPS. Instead, the reduced region appears to have an amorphous structure composed of a network of bright lines. Although it shows no periodic structure, the bright rows appear to be oriented preferentially in the same directions as the rows of the MR structure. Although the resolution of the images of 20 are worse than in Figure 21, the same features can be seen. Considering that the XPS indicated two types of oxygen atoms on the reduced surface, one from the MR at 530.0 eV and one unknown at 529.7 eV, it appears that the amorphous structure contains oxygen corresponding to the latter component, though it is not clear how, exactly, it is incorporated.

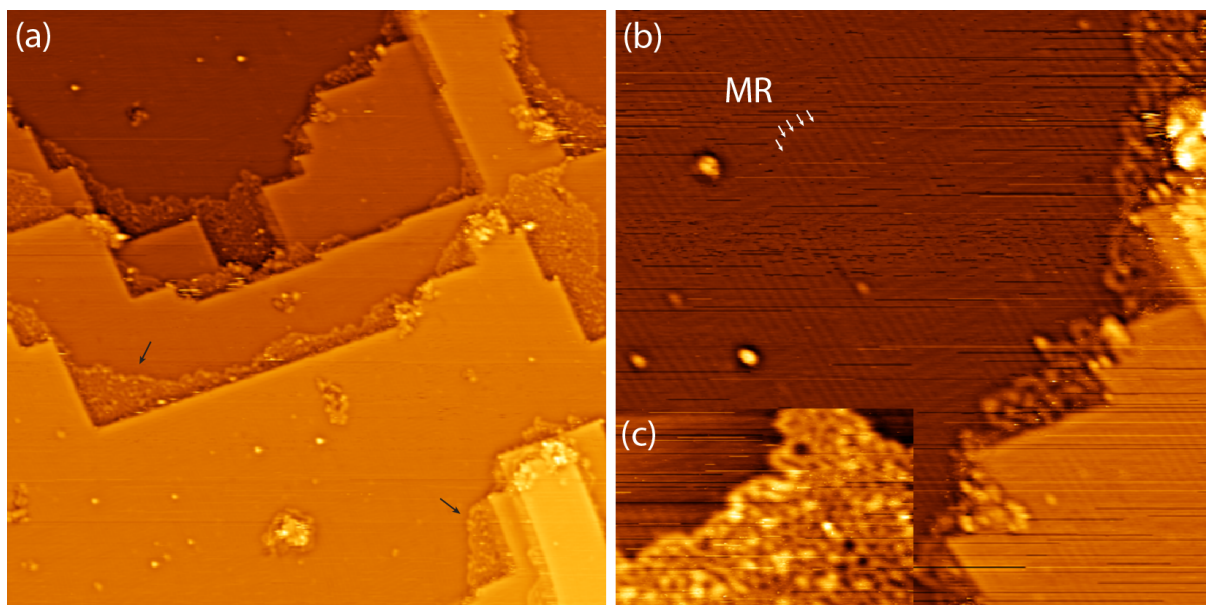


Figure 20: STM images of the reduced surface with an overall oxygen coverage of 0.44 ML, as determined by AES. The blue arrows in (a) indicates the reduced regions and the white arrows in (b) shows the rows in the MR structure on the terraces. (a) is 80x80 nm in size while (b) is 30x30 nm and (c) is 20x10 nm. The sample-tip bias is 1.5 V and the tunneling current is 200 pA.

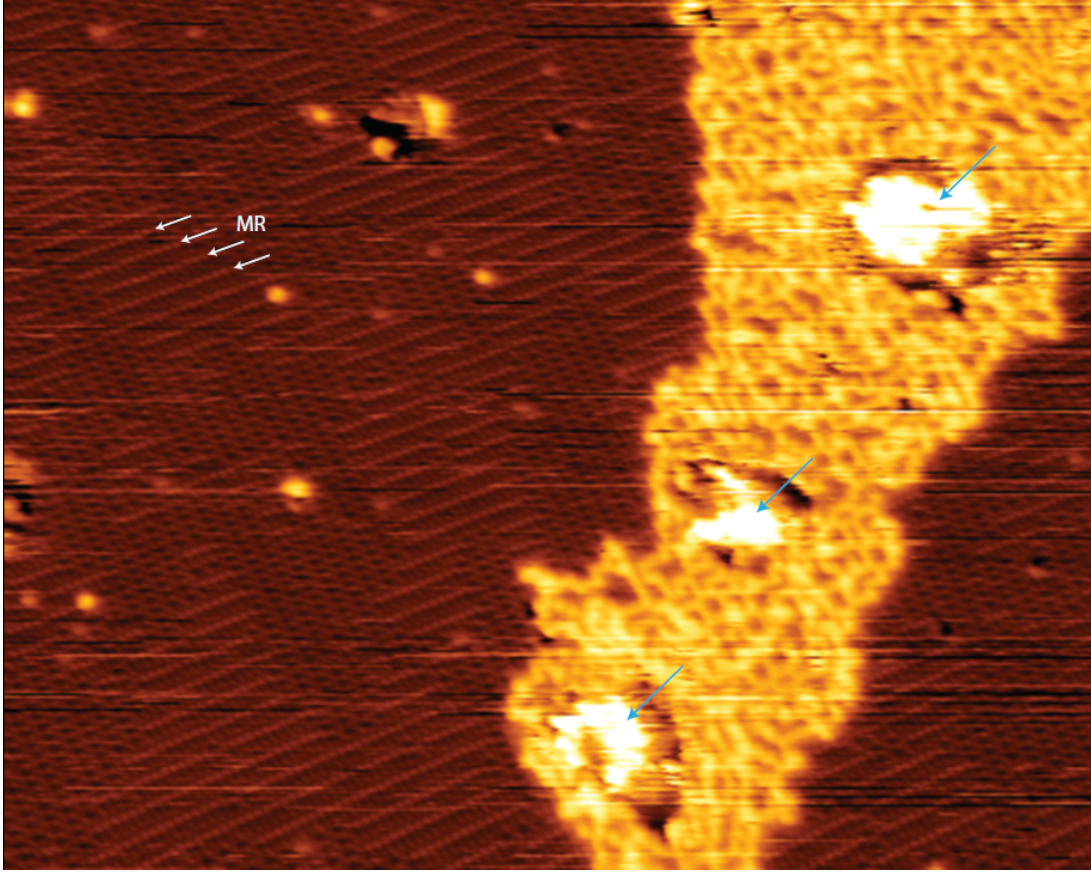


Figure 21: STM image of the reduced surface with an oxygen coverage of 0.44 ML. The blue arrows indicates the defects and the white arrows shows the rows in the MR structure. The second domain, perpendicular to the white arrows, of the MR structure looks different, which is explained by an asymmetric tip. The sample-tip bias is 1.5 V and the tunneling current is 200 pA.

To estimate the oxygen coverage of the surface imaged by STM the corresponding AES data are analyzed. The surface in Figure 21 has a ratio of the oxygen and copper peak, as illustrated in Figure 16, of $r_{reduced} = 0.15$. This gives an oxygen coverage of

$$\frac{0.15}{0.17} \cdot 0.5 \approx 0.44 \pm 0.02\text{ML}$$

The surface was reduced by approximately 10%. The surface in Figure 20 was prepared by making two cycles of reduction with the same parameters as Figure 21, but no substantial difference was measured. It is not possible to achieve an accurate evaluation of the oxygen coverage in the reduced regions from Figures 20 and 21. This would require much larger areas to be imaged (which was not done).

The LEED image of the reduced surface characterized by STM is shown in Figure 22. The pattern does not show any additional spots as compared to that from the pristine MR, see Figure 14(b). In contrast to the LEED pattern acquired for the reduced MR structure during the XPS experiments, no reduction in spot sharpness or increase in background intensity could be detected. This is attributed to the fact that the surface was reduced to a much smaller extent, such that these changes are not strong enough to be visible.

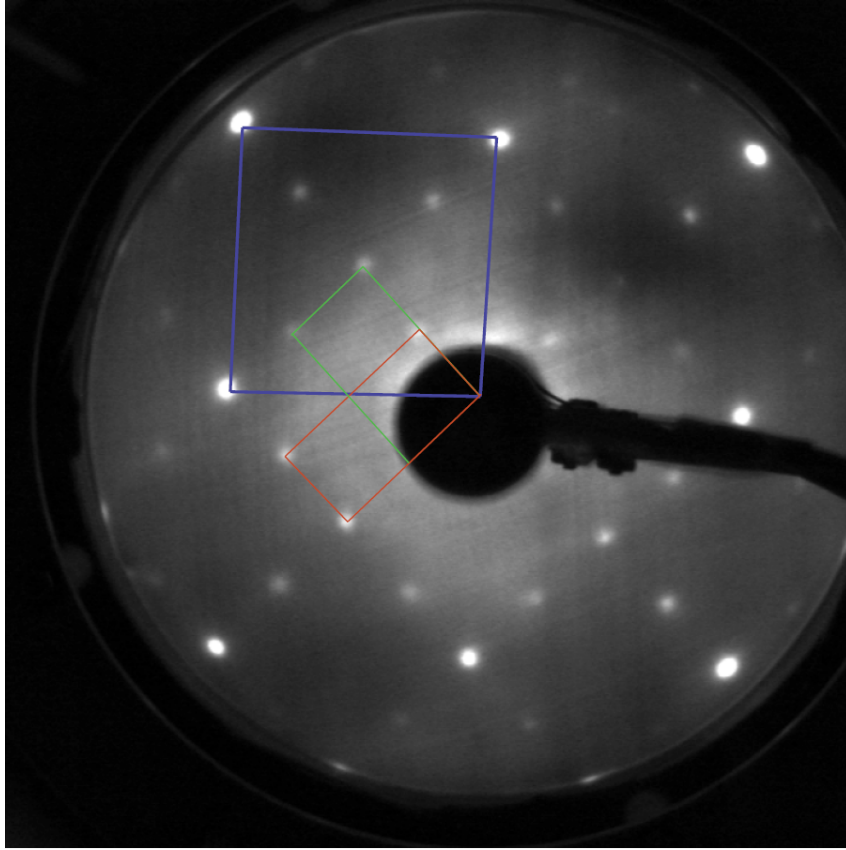


Figure 22: LEED image of the reduced surface corresponding to STM images in Figures 20 and 21. The image was acquired with an electron energy of 83 eV. Unit cells corresponding to the MR structure indicated with red and green rectangles.

5.2 CO₂ adsorption

To probe the chemical properties of the copper surface in various states of oxidation, adsorption experiments were conducted by dosing CO₂ at 100 K and characterizing the surface by XPS. O1s and C1s spectra acquired after CO₂ adsorption are summarized in Figure 23, where adsorption on the bare Cu(100) is compared with that on the MR structure and on a partially reduced surface.

The O 1s spectrum from bare Cu(100) shows new peaks at 531 eV and 533 eV, which according to literature could correspond to chemisorbed CO₂ (or CO₂^{δ-}, 531 eV) [29, 30], H₂O (533 eV) [31] and/or CO (532.8 eV) [32, 33, 34] on the surface. The peak at 533 eV fits well with the binding energy of CO on Cu(100). However, if CO exists on the surface it is reasonable to assume that CO₂ has dissociated to CO and O, but a peak due to atomic oxygen at 529.7 eV is missing from the spectrum [21, 31]. This can be explained by the existence of water on the surface, which probably comes from the background and sticks to the surface when the sample is cooled down. The X-ray beam tends to dissociate water to OH and H, where the H can react with O to form OH that appear at a binding energy of 531 eV [35]. Therefore, it is proposed that the peak at 531 eV is a mixture of chemisorbed CO₂ and OH and the peak at 533 eV is mixture of water and CO.

Further evidence of the interpretation of the O 1s spectrum can be seen from the C 1s spectrum, which has four distinct peaks with the binding energies of 284.4 eV, 286.2 eV, 287 eV, and 288.5 eV. The peak at 284.4 eV was already present before the CO₂ exposure and are, therefore, said to be contamination, which was a large problem while dosing gasses. The other three peaks at 286.2 eV, 287 eV and 288.5 eV, are according to literature suggested to be CO (286.2 eV) [32], formate (HCOO, 287 eV) [31], chemisorbed CO₂ (288.5 eV) [29, 30]. Formate is not expected when the surface is only exposed to CO₂, there is no source of hydrogen, but it can be explained by the presence of water on the surface. The water, or the atomic H from the dissociation, can be thought to interact with CO₂ to form formate. This is supported by previous studies on polycrystalline copper exposed to CO₂ and H₂O [31]. Thus, the formate further supports the existence of water on the surface. Formate should, however, show up in the O 1s spectrum at around 531.4 eV, but it is most likely hard to deconvolute due to the large noise in the spectrum.

It is possible that the peak at 531 eV is an effect of the X-ray beam. The physisorbed CO₂ will completely desorb at a higher temperature, approximately 160 K, while the chemisorbed CO₂ still stick on the surface. V.M. Browne, et. al., have shown that if a spectrum is measured while the surface is at 80 K and the surface is then heated above 160 K there will be a small peak from the chemisorbed CO₂. However, if the surface is directly heated, without doing a measurement, above 160 K there will be no chemisorbed CO₂ peak. The conclusion was that the creation of CO₂^{δ-} is induced by the beam [36].

The C 1s and O 1s spectra of the MR structure after it was exposed to 10 L of CO₂ at -160 °C can be seen in Figure 23(b). The fitting of the O 1s spectrum was performed by fixing all the peak positions and shapes corresponding to the MR structure itself from the fit shown in Figure 17, any features which could not be fitted in this way are attributed to adsorbates. It can be seen from the figure that three new peaks have appeared at 529.5 eV, 533.7 eV and 534.6 eV. The large peak at 534.6 eV can be attributed to physisorbed CO₂, with the reason that the adsorbed CO₂ has been found on other copper surfaces at larger binding energy than other oxygen species [36, 29, 37]. The peak at 533.7 eV is assigned to water, although, the peak has shifted from 533 eV. The peak at 529.5 eV is unknown and probably an effect from the method of fitting the peaks. The peak from the MR, and its shake-up peak, was fixed as they were before the CO₂ exposure and if the peaks would change after the exposure it could be expected that peaks appear or is shifted.

The C 1s spectrum has five peaks at 291.1 eV, 288.5 eV, 287.8 eV, 284.4 eV and 283.2 eV. The peaks at 284.4 eV and 283.2 eV were already present on the clean surface, although much smaller, and therefore are assigned to contamination (atomic carbon or hydrocarbons). The peak at 291.1 eV is assigned to physisorbed CO₂ by the reason that it has a larger binding energy than the other expected carbon species [37, 29, 36]. Furthermore, physisorbed CO₂ do not exist on the clean surface after exposed to CO₂, in contrast to the MR. From exclusion principle, the peak at 291.1 eV can be assigned to physisorbed CO₂. The peak at 287.8 eV is assigned to formate, although it has shifted by 0.7 eV if compared to Figure 23(a), which could be from different adsorption geometry.

The C 1s and O 1s spectra of the partly reduced MR after it have been exposed to 10 L of CO₂ at -160 °C can be seen in Figure 23(c). The O 1s spectrum was fitted in the same way as for the O 1s spectrum in Figure 23(b). It can be seen from the figure that three new peaks have appeared, at 531 eV, 533.2 eV, and 534.6 eV, which is assigned to

chemisorbed CO₂ and OH (531 eV), H₂O and CO (533.2 eV), and physisorbed CO₂.

The C 1s spectrum contains six peaks at 291.1 eV, 288.2 eV, 286.7, 286.3 eV, 284.1 eV and 282.5 eV. The peaks at 284.1 eV and 282.5 eV were already present before dosing CO₂. The peak at 288.2 eV are close to the chemisorbed CO₂ on the clean surface and, therefore, attributed to CO₂. The peak at 286.7 eV is attributed to formate and 286.3 eV to CO.

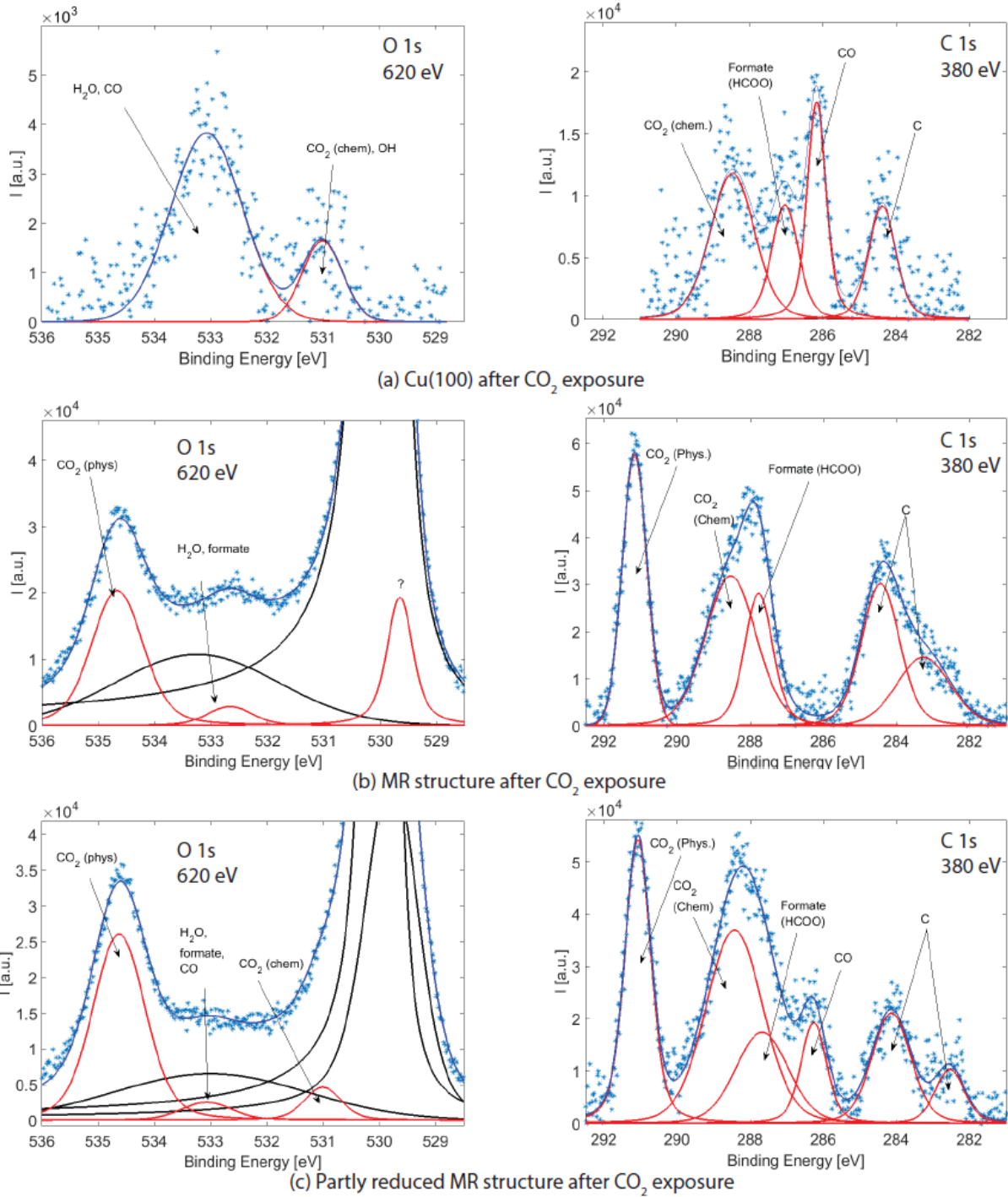


Figure 23: O 1s and C 1s spectra after Cu(100) (a), MR (b), and partly reduced MR (c) are exposed to CO₂. The O 1s spectra are in the left panel while the C 1s on the right. The red peaks are peaks fitted to the spectrum while the black peaks were fixed. The blue line is the summed intensity from the peaks and the blue dots are the measured data.

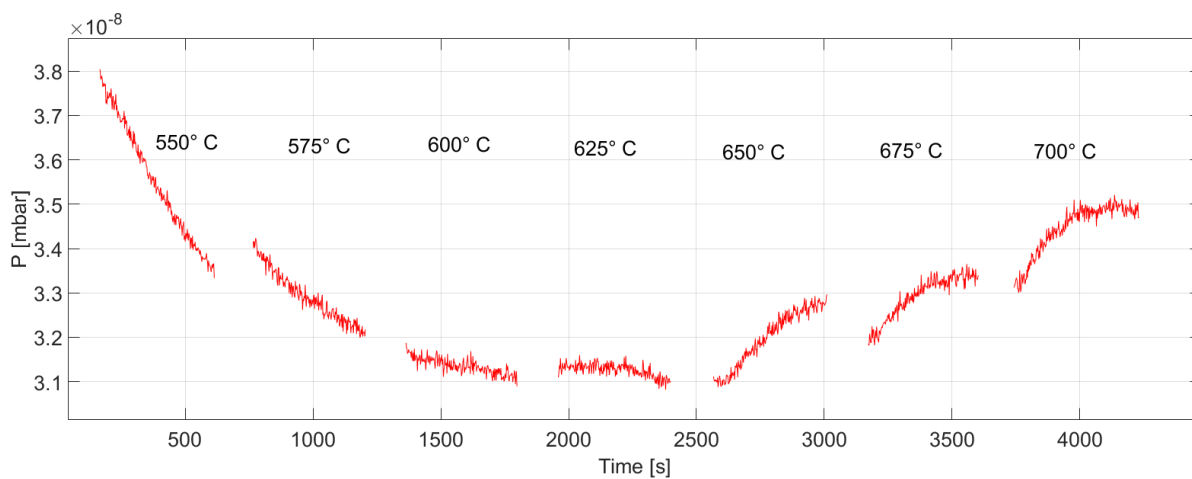
		O1s	C1s
1	H ₂ O	533 eV	
2	CO ₂ (phys)	534.6 eV	291.1 eV
3	CO ₂ (Chem)	531 eV	288.2-288.5 eV
4	CO	533 eV	286.2-286.3 eV
5	Formate	~ 531.4 eV	286.7-267.8
6	Atomic carbon/hydrocarbons		282.5-284.4
7	OH	~ 531eV	

Table 1: Table for the assigned peaks in Figure 23.

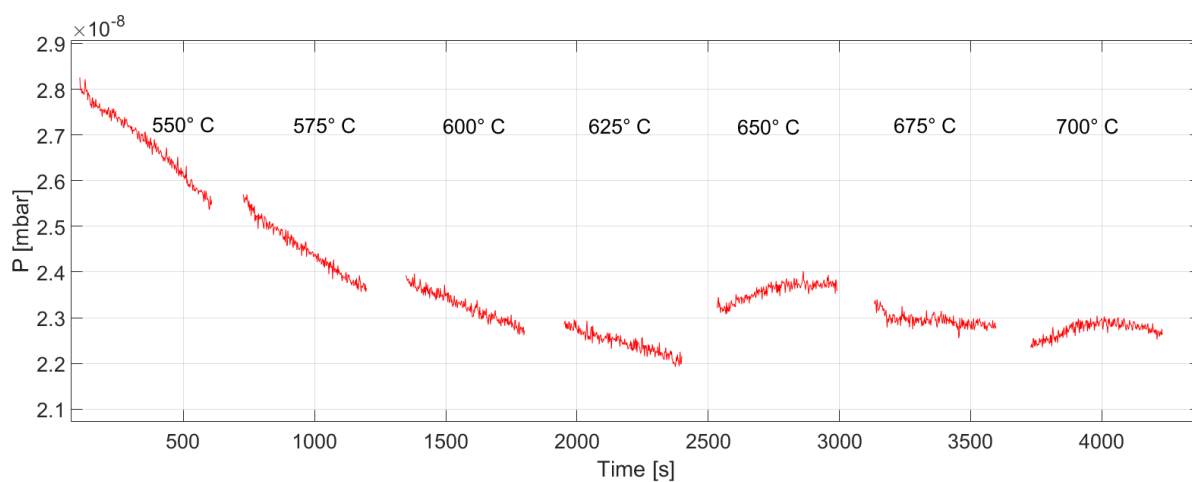
5.3 Catalytic Activity

As described in Section 4, as a complementary project to the ultra-high vacuum surface science investigation described above, preliminary tests of the catalytic activity of the Cu(100) crystal under realistic RWGS conditions were conducted. Eventually, this type of measurement is expected to serve as a bridge linking the surface science and with the behavior of the real industrial catalysts.

The result from the flow reaction experiment can be seen in Figure 24(a). The gas mixture of CO₂/H₂ was flowed through the reactor cell. When the signal from the RGA was stable the flow was stopped for approximately 10 min. The flow was started again and the temperature increased by 25 °C. This iteration was done until a temperature of 700 °C. Only the signal from CO is plotted, where the signal when the flow was on is cut out. All gas signals go down until 650 °C, where it can be seen that the CO signal increases modestly. However, there is no other molecule which increases in pressure. The result from the blank test is shown in Figure 24(b). It can be seen that the CO signal decreases until 650 °C. At 650 °C the signal increases, however, the increase is smaller than with the copper sample.



(a) Cu(100)



(b) Blank test

Figure 24: Activity measurement of with (a) the Cu(100) sample and (b) a blank test. The CO signal is plotted vs. time in both (a) and (b). The temperatures are indicated for every region. The data when the flow is on are cut out. The gas flow was 15 ml/min CO₂ and 15 ml/min H₂. The pressure in the reactor cell is 100 mbar.

6 Discussion

From the first experiment it was seen that when the MR was reduced by H_2 a new phase appeared at the step edges and at defects. The structure of the new phase cannot be determined by the STM and XPS results alone. One can only speculate about the structure based on the data available. As discussed above, it seems that the reduced regions have an amorphous structure. If the oxygen were completely removed from the MR structure the surface would consist of a layer containing 0.75 ML of copper. The reduced regions could, in principle (assuming that kinetic limitations prevent conversion back to the smooth (1x1) Cu(100)), form a pure copper structure with 25% vacancies. The XPS data, however, showed two O 1s peaks for the reduced surface, one from the MR and one unknown peak. It is, therefore, clear that the reduced regions contain chemisorbed oxygen. It could be that this residual oxygen prevents rearrangement of atoms in the reduced regions to form an ordered structure.

The most reduced surface that was imaged by STM had an oxygen coverage of approximately 0.44 ML. Ideally, one would want to image a more reduced surface for better comparison with the XPS results. It could be possible that an intermediate ordered structure appears at lower coverage than was reached in the STM experiments. The STM experiments are therefore not complete and more work has to be conducted to obtain a better understanding of the surface structure in the reduction process by H_2 .

As mentioned in the background there is a phase transition between the ordered Cu-vacancy structure, the missing row reconstruction, and a disordered Cu-vacancy structure at approximately 473 K (200 °C). Although the temperature during reduction is overestimated in the STM experiments, it is safe to assume that the temperature was above 200 °C. This implies that the reduction reaction did not take place on the MR, but instead on the disordered Cu-vacancy surface. The problem is that the surface cannot be studied in situ at 200 °C K with the setup used in this work. The surface converts back to the MR after the sample has cooled down. It is, therefore, unclear what role the MR structure might play in catalysis.

The results from the CO_2 adsorption experiment indicate that CO_2 does not fully adsorb on the clean Cu(100) surface. It seems, instead, that oxygen on the surface causes CO_2 to adsorb more extensively. There were differences between the MR and the reduced MR. From Figure 23 it is evident that CO exists on the reduced surface. However, CO does not form on the MR structure. It is concluded, therefore, that the difference between the interaction of CO_2 with the different surfaces originates from the reduced regions, where it seems that CO_2 adsorbs dissociatively, similarly to on bare Cu(100).

There are several features in the XPS spectra that are uncertain. For example, the peak at 529.5 in the O1s spectrum of CO_2 adsorbed on the pristine missing row structure (Figure 23(b)) is not present on the reduced surface. A possibility is that this peak is an artifact of the fit procedure where the main peaks from the MR structure were assumed to be constant. A small shift in the position or a change in the width of this peak could give rise to an error which is compensated by this new peak. The broad satellite peak at 533.3 eV obscured a large part of the spectra, complicating the fitting. However, if the fitting is assumed to be correct the differences between the interaction of the MR and reduced MR with CO_2 are interesting and should be further investigated.

There was a clear contamination of H₂O and atomic carbon on the surface in the XPS experiments. The effect of these contaminants is not fully understood. Formate was observed on the surface after CO₂ exposure. This makes no sense if there are no sources of hydrogen. H₂O is expected to have caused the formate to form on the surface. Other effects of the contaminants are unknown.

The relevance of the XPS results for the reactions discussed in the introduction can be debated. The conditions under which the experiments were conducted are not realistic for the reactions of interest. The results show differences in the interaction of CO₂ with the different surfaces. The trends observed should in principle be reflected similarly at higher temperatures and pressures. For example, even under realistic conditions, CO₂ should have a higher sticking probability on the oxygen-rich surface than on clean copper. The fact that the MR structure becomes disordered at high temperature complicates extrapolations. However, chemically the disordered c(2×2) surface with 25% Cu vacancies should not be drastically different from the MR structure. Many oxygen atoms in the disordered c(2×2) structure should be coordinated to 3 copper atoms, similar to the MR. That the disordering to the c(2×2) does not in fact have important effects on the reactivity is not known and should be investigated further.

The in-situ reactivity experiment showed that there is a slight increase in the CO signal at 650 °C. It is unclear from the measurements if the sample become active or not. The increase in the CO signal could be from a leak. The flow reactor during the experiment and at a point, it is possible that the leak becomes larger. The problem with a leak from the atmosphere is that N₂ have the same mass as CO. Although, the increase in CO is more distinct with the copper sample. However, the results show that the reactor cell can be used for future in-situ surface X-ray diffraction experiments.

7 Outlook

Several conclusions from the thesis work can be made. It was found that the reduction of the MR structure takes place at step edges and at defects. Specifically, the reduction of the MR seems to propagate at the lower terrace of the step edge. CO_2 was found to stick more readily on the oxidized surface compared to clean Cu(100). This would suggest that the surface should be more active for the RWGS reaction if it contains oxygen. However, as mentioned in the result and discussion there are many things that are still unclear. To investigate the subject further four experiments are proposed:

- High-Pressure X-ray Photoelectron Spectroscopy (HPXPS). With HPXPS, it is possible to make in-situ XPS measurements of the surface under more realistic temperature and pressure conditions. With a higher pressure and temperature, it would, for example, be possible to investigate the role of the disordered $c(2 \times 2)$ structure in the catalytic reactions.
- Further investigations of the reduced surface with STM. The surface was only reduced to app. 0.44 ML oxygen coverage. This should be continued to lower oxygen coverages. It would also help to record images with better resolution, so that more detailed information about the atomic structure can be obtained.
- In-situ STM. It is possible to conduct STM experiment under more realistic conditions. It would be beneficial to image the surface at a higher temperature and even during the reduction of the MR, providing more insight into the process.
- In-situ Surface X-ray Diffraction. Although under realistic conditions the surface is covered in a disordered $c(2 \times 2)$ structure, which may be difficult to detect, an in-situ Surface X-ray Diffraction experiment could be useful. The first experimental evidence for the $c(2 \times 2)$ structure was obtained from an in-situ SXRD experiment. It is, therefore, possible that useful structural information can be extracted from such measurements during operation of the crystal as a RWGS catalyst.

Acknowledgments

Foremost, I would like to give special thanks to my supervisors, Johan Gustafson and Lindsay R. Merte, for the guidance, discussion and encouragement they have given me through the work. Without their support, this thesis would not exist. I also wish to express gratitude to Andreas Schaefer and Prof. Edvin Lundgren for providing discussion, assistance, and support. I wish also to thank Estephania Lira, Milena Moreira, Mikhail Shipilin, Jovana Colvin, Jan Knudsen and Alif Arman for helping me in the laboratory.

References

- [1] W. Wang, S. Wang, X. Ma and J. Gong, *Recent advances in catalytic hydrogenation of carbon dioxide*, Chem. Soc. Rev., **40** (2011), 3703-3727.
- [2] M. D. Porosoff, B. Yanb and J. G. Chen, *Catalytic reduction of CO₂ by H₂ for synthesis of CO, methanol and hydrocarbons: challenges and opportunities*, Energy Environ. Sci., **9** (2016), 62-73.
- [3] HALDOR TOPSOE, LK-801, Low temperature shift catalyst, <http://www.topsoe.com/products/lk-801>, 5/9/2016.
- [4] C.S. Chen and W.H. Cheng, *Study on the mechanism of CO formation in reverse water gas shift reactions over Cu/SiO₂ catalyst by pulse reaction, TPD and TPR*, Catalysis Letters, **83** (2002), 121-125.
- [5] F. Yang, Y. Choi, P. Liu, J. Hrbek, and J.A. Rodriguez, *Autocatalytic Reduction of a Cu₂O/Cu(111) Surface by CO:STM, XPS, and DFT studies*, J. Phys. Chem. C, **114** (2010), 17042–17050.
- [6] T. Matsumoto, R.A. Bennett, P. Stone, T. Yamada, K. Domen, and M. Bowker, *Scannign tunneling microscopy studies of oxygen adsorption on Cu(111)*, Surf. Sci., **471** (2001), 225-245.
- [7] G. Attard and C. Barnes, *Surfaces*, OXFORD SCIENCE PUBLICATIONS.
- [8] P. Hofmann, *Surface Physics: An Introduction Written*, version 1.3.
- [9] A. Grob, *Theoretical Surface Science: A Microscopic Perspective*, Springer, second edition.
- [10] C. Gattinoni and A. Michaelides, *Atomistic details of oxide surfaces and surface oxidation: the example of copper and its oxides*, Sur. Sci. Rep., **70** (2015), 424-447.
- [11] F. Besenbacher and J.K. Nørskov, *Oxygen chemisorption on metal surfaces: general trends for Cu, Ni and Ag*, Prog. Surf. Sci. **44** (1993), 5-66
- [12] K. Lahtonen, M. Hirsimäki, M. Lampimäki, and M. Valden, *Oxygen adsorption-induced nanostructures and island formation on Cu100: Bridging the gap between the formation of surface confined oxygen chemisorption layer and oxide formation*, J. Chem. Phys., **129** (2008), 124703.
- [13] M. Wuttig, R. Franchy and H. Ibach, *Oxygen on Cu(100) - a case of an adsorbate induced reconstruction*, Surf. Sci., **213** (1989), 103-136.
- [14] M. Kittel, M. Polick, R. Terborg, J.T. Hoeft, P. Baumgärtel, A.M. Bradshaw, R.L. Toomes, J.H. Kang, D.P Woodruff, M. Pascal, C.L.A. Lamont and E. Rotenberg, *The structure of oxygen on Cu(100) at low and high coverages*, Surf. Sci., **470** (2001), 311-324
- [15] K.-I. Tanaka, T. Fujita and Y. Okawa, *Oxygen induced order–disorder restructuring of a Cu(100) surface*, Surf. Sci., **401** (1998), 407-412.
- [16] M.Z. Baykara, M. Todorovic, H. Monig, T.C. Schwendemann, O. Unverdi, L. Rodrigo, E.I. Altman, R. Perez, and U.D. Schwarz, *Atom-specific forces and defect identi-*

- fication on surface-oxidized Cu(100) with combined 3D-AFM and STM measurements*, Phys. Rev. B, **87** (2013), 1-9.
- [17] M. J. Harrison, D. P. Woodruff, and J. Robinson, *Adsorbate-induced surface reconstruction and surface-stress changes in Cu(100)/O: Experiment and theory*, Phys. Rev. B, **74** (2006), 165402.
- [18] M. Lampimäki, K. Lahtonen, M. Hirsimäki, and M. Valden, *Nanoscale oxidation of Cu(100): Oxide morphology and surface reactivity*, J. Chem. Phys., **126** (2007) , 034703.
- [19] H. Iddir, D.D. Fong, P. Zapol, P. H. Fuoss, L. A. Curtiss, G.-W. Zhou, and J.A. Eastman, *Order-disorder phase transition of the Cu(001) surface under equilibrium oxygen pressure*, Phys. Rev. B, **76** (2007), 2-5.
- [20] I.K. Robinson, E. Vlieg, and S. Ferrer, *Oxygen-induced missing-row reconstruction of Cu(001) and Cu(001)-vicinal surfaces*, Phys. Rev. B, **42** (1992), 6954-6962.
- [21] H. Tillborg, A. Nilsson, B. Hernnhäs and N. Mårtensson, *O/Cu(100) studied by core level spectroscopy*, Surf. Sci., **270** (1992), 300-304.
- [22] s. Hofmann, *Auger- and X-Ray Photoelectron Spectroscopy in Materials Science: A User-Oriented Guide*, Springer.
- [23] P.S. Bagus, E.S. Ilton, and C.J. Nelin, *The interpretation of XPS spectra: Insights into materials properties*, Sur. Sci., **68** (2013), 273-304.
- [24] R. Nyholm, J.N. Andersen, U. Johansson, B.N. Jensen, and I. Lindau, *Beamline I311 at MAX-LAB: a VUV/soft X-ray undulator beamline for high resolution electron spectroscopy*, Nuclear Instruments and Methods in Physics Research A, **468** (2001) 520–524.
- [25] B. Voigtländer, *Scanning Probe Microscopy: Atomic Force Microscopy and Scanning Tunneling Microscopy*, Springer.
- [26] J. Thersoff and D.R. Hamann, *Theory of the scanning tunneling microscope*, Phys. Rev. B, **31** (1985), 805-813.
- [27] H. Tillborg, A. Nilsson, T. Wiell, N. Wassdahl, N. MArtensson, and J. Nordgren, *Electronic structure of atomic oxygen adsorbed on Ni(100) and Cu(100) studied by soft-x-ray emission and photoelectron spectroscopies*, Phys. Rev. B, **47** (1993), 464-470.
- [28] M. Okada, K. Moritani, S. Goto, and T. Kasai, *Actively controlled oxidation of Cu(100) with hyperthermal O₂ molecular beam*, J. Chem. Phys., **119** (2003), 6994-6997
- [29] H.-J. Freund and M.W. Roberts, *Surface chemistry of carbon dioxide*, Surf. Sci., **25** (1996), 225-273.
- [30] R.G. Copperthwaite, P.R. Davies, M.A. Morris, and M.W. Roberts, *The reactive chemisorption of carbon dioxide at magnesium and copper surfaces at low temperature*, Catalysis Letters, **1** (1988), 11-20.
- [31] X. Deng, A. Verdager, T. Herranz, C. Weis, H. Bluhm and M. Salmeron, *Surface Chemistry of Cu in the Presence of CO₂ and H₂O*, Langmuir, **24** (2008), 9474–9478.

- [32] P.R. Norton and R.L. Tapping, *Photoelectron spectroscopic studies of the adsorption of CO and CO₂ on nickel, platinum and copper*, Chem. Phys. L., **38** (1976), 207-212.
- [33] H. Tillborg, A. Nilsson and N. Mårtensson, *Shake-up and shake-off structures in core level photoemission spectra from adsorbates*, J. Electron Spectrosc. Relat. Phenom., **62** (1993), 73-98.
- [34] A. Sandell, P. Bennich, A. Nilsson, B. Hernäs, O. Björneholm, and N. Mårtensson, *Chemisorption of CO on Cu(100), Ag(110) and Au(110)*, Surf. Sci., **310** (1994), 16-26.
- [35] E. Cano, C.L. Torres and J.M. Bastidas, *An XPS study of copper corrosion originated by formic acid vapour at 40% and 80% relative humidity*, Materials and Corrosion, **52** (2001), 667-676.
- [36] V.M. Browne, A.F. Carley, R.G. Copperthwaite, P.R. Davies, E.M. Moser and M.W. Roberts, *Activation of carbon dioxide at bismuth, gold and copper surfaces*, Appl. Surf. Sci., **47** (1991), 375-379.
- [37] T. Koitaya, S. Yamamoto, Y. Shiozawa, K. Takeuchi, R.-Y. Liu, K. Mukai, S. Yoshimoto, K. Akikubo, I. Matsuda, and J. Yoshinobu, *Real-Time Observation of Reaction Processes of CO₂ on Cu(997) by Ambient-Pressure X-ray Photoelectron Spectroscopy*, Topics in Catalysis, **59** (2015), 526-531.